2020

Dynamic Loading Experimentation and Surface Imaging of Pressure Vessel Loadcell Fractures

Austin T. Sumner
Georgia Southern University

Dynamic Loading Experimentation and Surface Imaging of Pressure Vessel Loadcell Fractures

An Honors Thesis submitted in partial fulfillment of the requirements for Honors in Mechanical Engineering

By Austin Sumner

Under the mentorship of Dr. Aniruddha Mitra

Georgia Southern University
Statesboro, GA, USA
November 2020

ABSTRACT

Pressure vessels are very common pieces of equipment in industry and they are used for a variety of applications. It is standard in industry to rest pressure vessels on load cells. For some special cases, the pressure vessels are rested on load cells instead of solid foundation. Pressure vessels and their loadcells are generally designed for static environmental conditions and loading and tend to experience adverse effects when exposed to dynamic environments, such as hurricanes and earthquakes. These adverse-loading conditions cause vibrations and asymmetrical loading on the load cells, which can concurrently cause unexpected failure. This research investigates the effects of wind loading on three-legged industrial pressure vessels through experimental process and looks into the failure mechanisms of a failed load cell under wind loading. At the conclusion of this investigation a critical wind speed may be suggested for each type of pressure vessel under which the operating life of the loadcell can be affected significantly. This is measured through experimentation if a scaled-down pressure vessel shows signs of instability when exposed to an appropriate wind loading and only shows instability only in the worst-case scenario. Additionally, a surface imaging analysis of a fractured loadcell shows the nature in which this added wind loading effects the base on which the vessel rests. After reviewing the surface, it is determined that the fracture is ductile in nature and there are three stages of the fracture: an initial point of fracture, a propagation stage where the surface cracks grow and sink into the loadcell body due to continued fatigue loading and corrosion, and a final ductile failure of the loadcell geometry once it can no longer withhold its operational weight. This analysis shows that the primary cause of the surface cracking is a large quantity of low magnitude impacts coming from the pressure vessel leg when a dynamic wind loading is applied.

Thesis Mentor: _____

Dr. Aniruddha Mitra

Honors Director: _____

Dr. Steven Engel

TABLE OF CONTENTS

ACKNOWLEDGEMENTS

There are many people that this research could not be done without, and I extend my appreciation to each of them. I would like to first acknowledge the Mechanical Engineering department at Georgia Southern University, Johnson Matthey, and Keyence for their support throughout this project.

I want to extend a special thank you to Dr. Aniruddha Mitra, for without his leadership this project would not have been completed. He has been the best mentor throughout these years of research. Additionally, thank you to Dr. Brian Vlcek for use and training on the surface imaging techniques and Dr. Mosquefer Rahman for use of his subsonic wind tunnel laboratory.

Without the help and dedication of this research team, this project also may not have been as fruitful as it was. A special recognition goes to Seth Nowak for being the leader of the group and organizing the research team in a clear and effective manner. Joycee Bethapudi, Thomas Zidek, Ryan Ryder, Ashlyn Jackson, and John Havernar also helped immensely in this project and the combined brain power of all of us lead to the innovations and solutions that have made this project successful.

Finally, I would like to recognize my family and friends that have been with me through this process. Thomas and Tammy Sumner, Nathan Sumner, Johnathan Spathelf, Lucas Ogletree, Evan Butterworth, Max Ware, Tristan Fields, Noelle Anderson, Nicholas Jenkins, Kacie Grella, Meredith Eaheart, John Hyle, Shelby Husband, Larry Allen, Sara Martin and all others that have helped me throughout these four years of undergrad, for the list goes on. Without these peoples help, I am unsure where I would be today, and they are all greatly appreciated.

NOMENCLATURE

CUFT - Cubic Feet, Standard Unit of Volume in US Customary System

Inches – Standard Unit of Length in US Customary System

mph – Miles Per Hour, Unit of Speed in US Customary System

m – Mass, denoted in kg or lbm

ρ - density, given in kg/m^3

mu – Kinematic Viscosity

A - Amps, Unit of Electrical Current

ksi – Kilo-Pounds per Square Inch, Unit of Pressure in US Customary System

1. BACKGROUND INFORMATION

1.1 PRESSURE VESSEL

Pressure vessels are integral pieces of equipment that are used in a variety of ways in the industrial scape. Within this research, the main focus will be on large pressure vessels that are exposed to outdoor conditions for the majority of their functional life. There are three sizes of pressure vessel that will be analyzed: 50 Cuft, 200 Cuft, and 1100 Cuft. An example of a 200 Cuft pressure vessel is shown below in figure 1.1. The large cylindrical body perpendicular to the vertical direction is called a manway.

Figure 1.1: 200 Cuft Pressure Vessel

These pressure vessels are currently in use in the industrial world to hold two different fluids for different purposes: a catalyst and water. For the majority of operational time, it

holds the catalyst. And is roughly filled up 90% of the way, leaving only very minimal amounts of space between the top of the vessel and the top of the fluid. The pressure vessel is filled with water for roughly a day out of every month to perform tests and cleaning, but it is infrequent compared to the time the pressure vessel is filled with the catalyst. The pressure vessel is rarely completely empty. The weights of the vessel under each fill condition are shown in table 1.1 below.

Table 1.1: Pressure Vessel Weights Under Different Fill Conditions

	Empty Condition (lbs)	Catalyst-Filled (lbs)	Water Filled Condition (lbs)
50 Cuft	4,400	6,900	7,700
200 Cuft	9.383.6	21,623	24,600
1100 Cuft	31,000	86,000	92,000

The designs of modern pressure vessels include a manway to accompany the quick draining of fluids and allow an entry point for any internal maintenance that must be performed. The manway is the cylindrical body that comes from the side of the pressure vessel body. When the pressure vessel is in operation, manways are sealed, and a thick steel cover is applied to hold pressure. Manways have an interesting relationship with the loading as they represent the only irregularity within the geometry of the pressure vessel. Without the manway, the pressure vessel body would be entirely symmetrical. This weight imbalance will become a large consideration as the shift in the center of gravity will affect how the pressure vessel reacts to wind. More add-ons to the pressure vessel are parallel bars

Additionally, pressure vessels are constructed with parallel bracing bars on the legs to minimize vibrations in the legs in the wind loadings. These parallel bars connect the legs to each other and act as a support against excessive vibrations. As wind loading increases around the pressure vessel, the pressure vessel will begin to vibrate. Without the parallel bars, the legs will see the most effect of this vibration and end up fracturing if the natural frequency of the pressure vessel body reaches the vortex shedding frequency of the wind over the vessel. If the vortex shedding frequency reaches the natural frequency of the body, the body will begin to show signs of excessive vibration failure. (Clark 2018, 1)

With all of these considerations taken into account, the three pressure vessel sizes that are being investigated in this report are modeled below in figure 1.2. From left to right is the model in Solidworks of the 50 Cuft, 200 Cuft, and 1100 Cuft. Table 1.2 shows the major dimensions of the larger pressure vessels. The diameter in this table is the diameter of the pressure vessel body and the body height is the height of the pressure vessel body itself. The body height does not include the leg height.

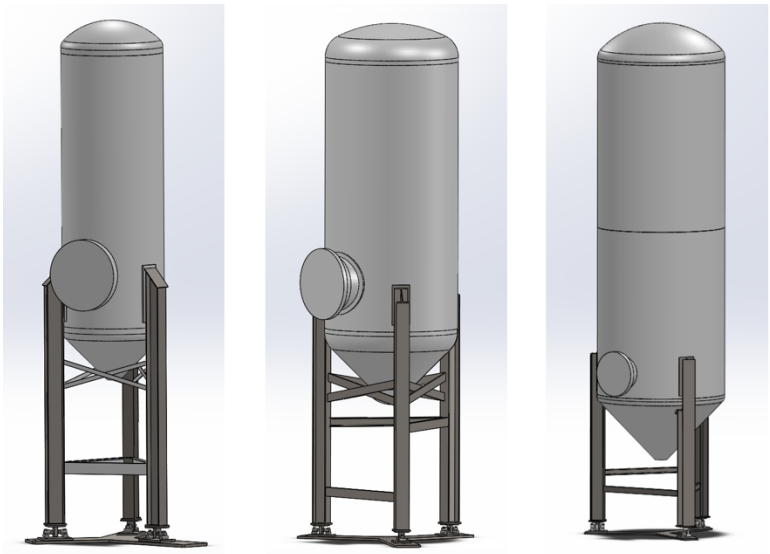

Figure 1.2: 50 Cuft, 200 Cuft, and 1100 Cuft CAD Models from SolidWorks

Table 1.2: Dimensions of Pressure Vessels			
Pressure Vessel	50 Cuft	200 Cuft	1100 Cuft
Diameter (Inches)	36	60	96
Body Height (Inches)	108	132.25	272

1.2 LOAD CELLS

The design of these pressure vessels has three legs which support the entire weight of the vessel. Load cells, or load measuring transducers, are resilient single-material devices that provide a load measurement with the help of a Wheatstone bridge and an electrical circuit comprising of reference resistors and capacitors. (Wolfendale 1) Each leg rests on a compression load cell made of 17-4 stainless steel, alloy 630 with the purpose of measuring the weight of the vessel as a measure of telling how full it is. Compression loadcells are called such because they measure and operate under a

compressive loading. Loadcells work because of strain gauges expertly placed within the geometry. Strain gauges are a precise measurement equipment that contain a fine wire within. As they are deformed, the resistance within the strain gauge is altered because resistance is a function of wire length and a quantifiable voltage change can be observed due to the mechanical deformation. As a compressive loadcell reacts to weight, the strain gauges produce a voltage differential that is proportional to the weight that is being added to the loadcell. This is how a loadcell measures weight. A 2D sketch of the theory of how the particular loadcells for this research works can be viewed below in figure 1.3. As shown here, these loadcells are simply supported on each end and the load is applied in the center of the structure. The strain gauge placements are marked with the orange marks.

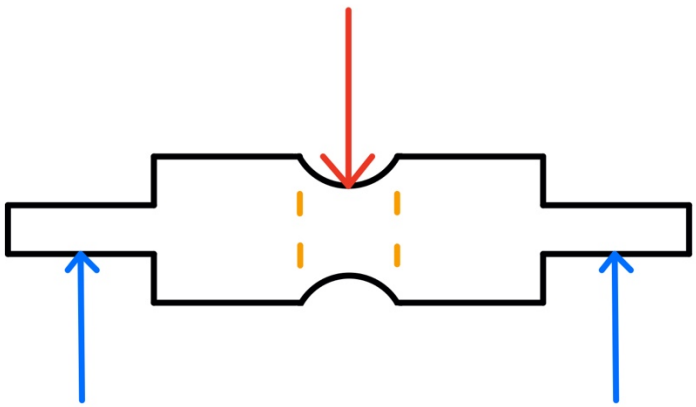

Figure 1.3: Loadcell Theory Illustration

As the loadcell deforms because of a weight, those internally positioned strain gauges will also change in length. It is important to note that the actual configuration for this type of loadcell requires a housing and bracket, shown in figures 1.4 and 1.6. The loadcell for the largest sized pressure vessel, the 1100 can be seen in figure 1.5. The

bracket rests on top of the loadcell where the red weight arrow is and connects to the pressure vessel leg.

Figure 1.4: 10,000 lb rated loadcell for 200 Cuft Pressure Vessel

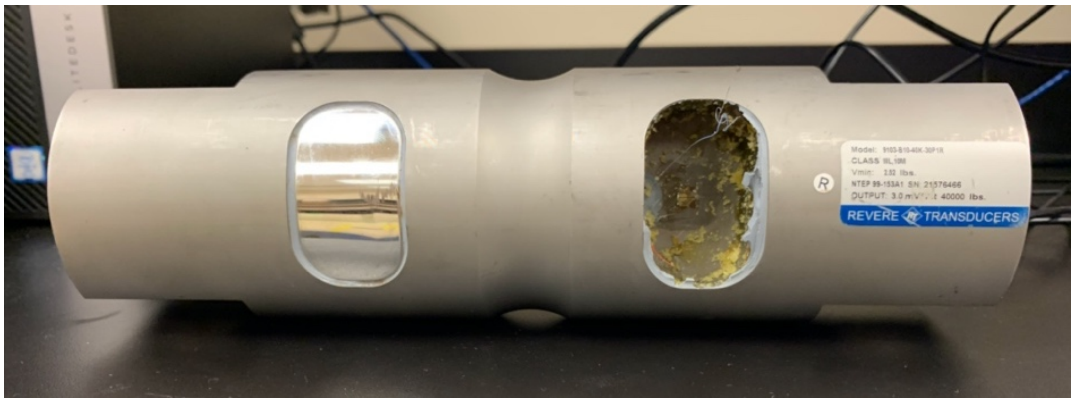

Figure 1.5: 40,000 lb rated loadcell for 1100 Cuft

As mentioned previously, there are 3 different pressure vessel sizes: the 50 Cuft, 200 Cuft, and the 1100 Cuft. These pressure vessel sizes need to use different loadcells rated for different ranges as they will constantly have differing weights within them. The

50 Cuft pressure vessel uses a 5,000 lb rated loadcell. The 200 Cuft pressure vessel uses a 10,000 lb rated loadcell. The loadcells used for the 50 Cuft and 200 Cuft pressure vessels are of the same dimensions. The 1100 Cuft pressure vessel uses a very large 40,000 lb rated loadcell.

The loadcell configuration can be seen below in figure 1.6 without the pressure vessel on top. It is very important to note that the loadcell is held into place by 2 pins, and there is about a 1/8-inch gap between the lower pin and the loadcell during normal operation. (Rice lake 2019, 1) Due to this, if a wind loading is able to push over the vessel, the loadcell will experience an impact due to this gap. The loadcell for the 50 Cuft and 200 Cuft pressure vessels are of the same geometry, while the loadcell for the 1100 Cuft pressure vessel is thicker.

Figure 1.6: Loadcell Configuration During Normal Operation

This research comes about after a loadcell failed while having a within-specification margin of safety. The hypothesis for the abrupt failure was that the pressure vessel was exposed to high-speed winds that caused an imbalance of weight among the

three pressure vessels either through many small impacts or a gradual rubbing force from the loadcell bracket on the loadcell itself.

The steps for proving was first to determine the failure type of the load cell through a surface imaging analysis and then to determine the effects of a wind loading on this pressure vessel. The purpose of the surface imaging segment of this paper is to decipher the clues that the fractured loadcell provides as to how the wind loading on the pressure vessel can be seen in the loadcells.

1.3 WIND EXPERIMENTATION FUNDAMENTALS

Additional loading applied by heavy winds on large pressure vessels is generally not accounted for when the structural integrity of a pressure vessel is being designed. A calculation process outlined in Appendix A finds theoretical wind speed values that would cause a toppling effect with the pressure vessel. This is the effect that is desired to view as when the pressure vessel begins to topple, the pressure vessel legs will have a discernable imbalance on the loadcells, supporting wind being the failure mode. The primary objective of this research was to design an experimental procedure to test and visualize the full effects of a dynamic wind loading on the structural stability of a pressure vessel. In doing so, a dimensional analysis is needed to be completed to scale down the experimentation to be able to test every required configuration.

A key component in completing this analysis is the use of the subsonic wind tunnel. The wind tunnel that is currently available to Georgia Southern University is a subsonic wind tunnel capable of producing wind speeds up to 30 mph. The wind tunnel is an open circuit wind tunnel which means that both ends are open. Environmental conditions are generally more turbulent than what is produced by this wind tunnel. This

type of wind tunnel produces laminar flow, which is good for this experiment because the goal is to simulate a strong wind moving in a specific direction making contact with a body within the airflow. Additionally, turbulent flow is very difficult to control and would lead to a significant amount of experimental error that cannot be accounted for.

Figure 1.7: Subsonic Wind Tunnel at Georgia Southern University

A CFX analysis was performed to create a velocity profile for this wind tunnel. This CFX analysis is shown below in figures 1.8, 1.9, and 1.10. Figure 1.8 shows a velocity vector field for the wind moving through the tunnel when the tunnel is running at 100% capacity; the wind speed is 30 mph. It can be seen through the vector field that as the air travels through the wind tunnel, it smooths out through the entire run and in the widening, and then speeds up in a very laminar fashion right in front of the exit and into the testing zone. The velocity contour plot is viewed in figure 1.9. The behavior of the wind through the tunnel can be seen here as well. Figure 1.10 shows the turbulence-kinetic energy within the wind tunnel to understand the type of flow producing. As can be

seen through that plot, the flow through the wind tunnel does not have a lot of turbulence within it and is producing very laminar flow, especially around the outlet.

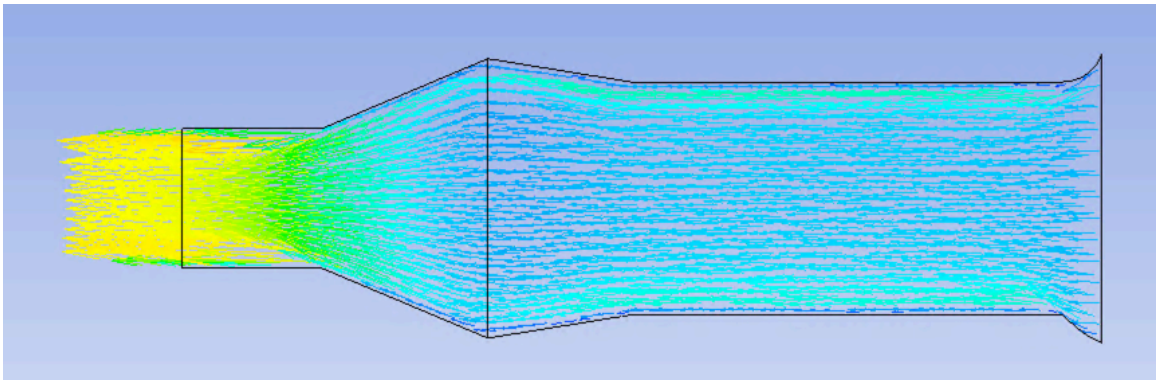

Figure 1.8: Velocity Vector Profile of Air Inside the Wind Tunnel in ANSYS CFX

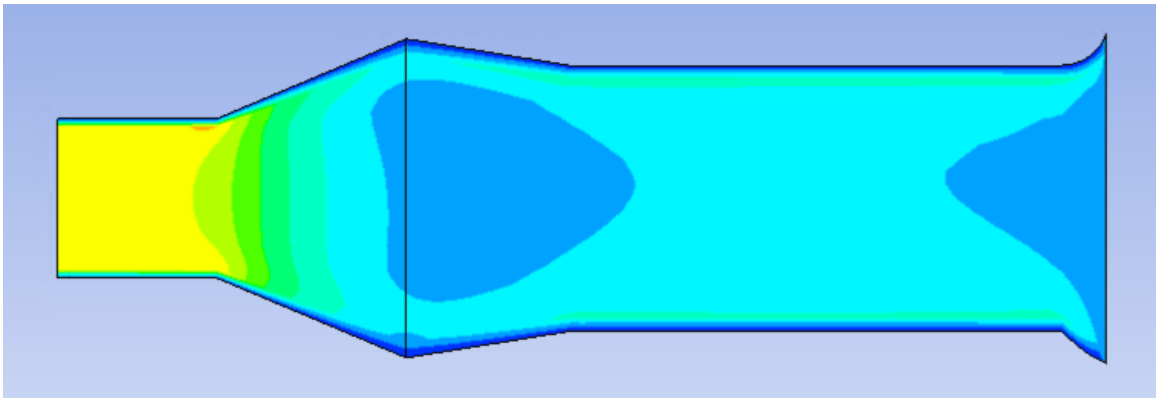

Figure 1.9: Velocity Contour Plot of Air Flow Through the Wind Tunnel in ANSYS CFX

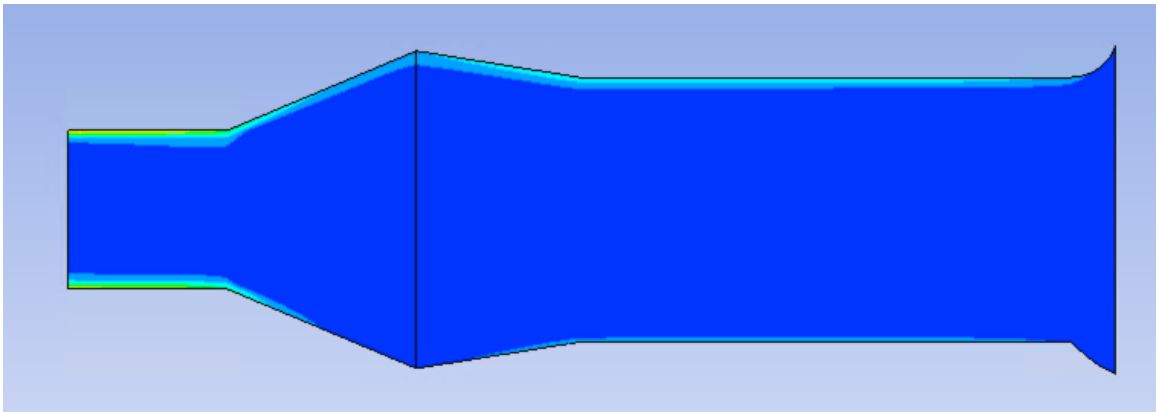

Figure 1.10: Turbulence Kinetic Energy Profile of Air Inside the Wind Tunnel in ANSYS CFX

Dimensional analysis is the process in which engineers go through to scale down an otherwise very large-scale experiment. As performing these experiments would be a very difficult task that would require immense preparation and precise timing on a full-sized pressure vessel, it is necessary to scale down the models so that the experiment can be performed on a variety of configurations with relative ease. When performing experiments like these, the main way to confront a dimensional analysis problem is to find relationships between the governing parameters for the phenomenon being researched. (Barenblatt 1996) In this case, it is very large pressure vessels that are needed to be scaled down. Dimensional analysis requires that at least one dimensionless number is manipulated to make a proper dimension. The Reynolds number was chosen here and is the basis for all wind velocity calculations. Equation 1 below is the equation for the Reynolds number.

$$Re = \frac{\rho * V * D}{\mu} \qquad [1]$$

After reviewing these values, a few very important assumptions must be made. Firstly, the kinematic viscosity, represented by the Greek letter mu, and the density, represented by the Greek letter ρ, can be assumed the same between the model and the actual pressure vessel as both are air and the climates, regarding humidity and pressure, are very similar between the testing environment and the location where these pressure vessels reside. D is the diameter of the pressure vessel body and V is the fluid velocity. Using these assumptions, an equivalency between the pressure vessel itself and the pressure vessel model is shown in equation 2. This is the base equivalency for calculating the wind speed values.

$$(VD)_{Pressure\ Vessel} = (VD)_{Model} \quad [2]$$

Assuming 120 mph as the velocity for the pressure vessel and the diameters listed above in table 1.2 and 30 mph as the highest possible wind velocity for the model, the diameter values for the model can be found and are shown in table 1.3 below. The next parameter needed is the height of the vessel. This can be given by looking at the testing site. The wind tunnel has an opening of 24 inches by 24 inches where the testing will take place. In order to have the most realistic testing zone, the height of the center of gravity should be around the center of air flow, which means the total height of the vessel should be 18 inches. An 18-inch total height of the model is ideal as a solidworks analysis provided the center of gravity for these pressure vessels is roughly 2/3 of the height of the pressure vessels. 2/3 of 18-inches is 12 inches, which is directly in the center of the wind tunnel opening. The proportion of the body height to the leg height is scaled down by 10 from the actual pressure vessels, whose models can be seen above in figure 1.2. The dimensional comparison between the smaller models and the larger models can be seen

below in table 1.3. It is important to note that the body height is not the total height, the body height does not include the height of the legs.

Table 1.3: Dimensions of 18-Inch Model Pressure Vessels			
Pressure Vessel	50 Cuft	200 Cuft	1100 Cuft
Diameter (Inches)	3.65	4.77	4.72
Body Height (Inches)	10.95	10.52	13.37

A sprayable rubber sealant was used on these 18-inch models to minimize their porosity and ensure that the wind will behave as it would in a steel-walled pressure vessel. Figure 1.11 below shows the 18-inch models before the application of the rubber sealant and the parallel bars. These photos are placed here to show the geometry. Figure 1.12 shows the final pressure vessel models used for experimentation.

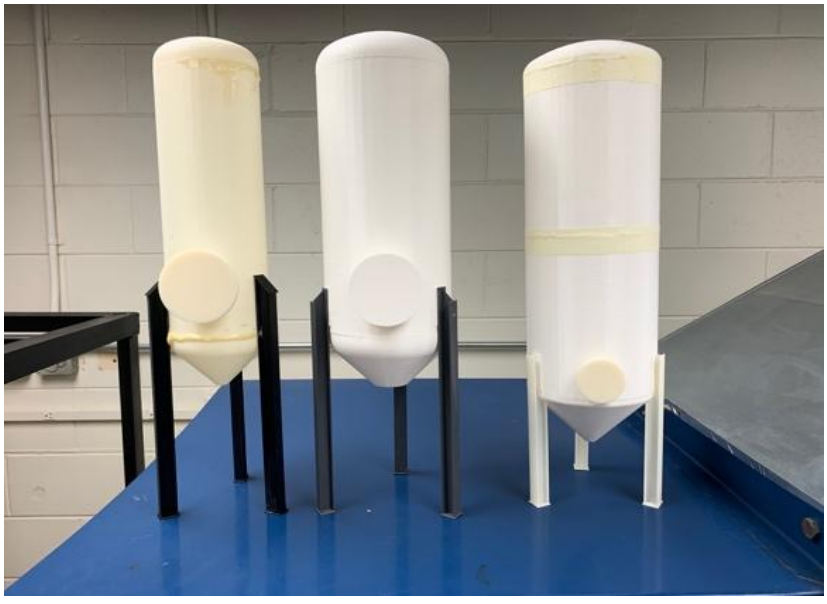

Figure 1.11: 18-Inch Scaled Down Pressure Vessel Models

Figure 1.12: 18-Inch Pressure Vessel Models Used For Experimentation

These pressure vessels will be used to conduct the proof of concept tests and prove the theoretical values outlined in Appendix A.

These pressure vessels will be tested in multiple conditions to prove the theoretical numbers are accurate. The first tests that will be run are the pressure vessels in the empty condition just to prove the experiment works and the empty conditions are accurate. Another test that should be performed after the all empty tests to view the effects of a filled condition rather than an empty condition pressure vessel against the wind loading. This is practical because the pressure vessel spends the bulk majority of its time in the catalyst-filled condition, therefore it will likely be under wind loadings with some mass inside of it. In addition to performing dimensional analysis to determine the size of the legs for the scaled down vessels, a mass ratio determination is to be performed to find a suitable replacement for the catalyst within the scaled-down vessel. The

following equation, equation 3, was derived to find a suitable replacement for the catalyst. The derivation of this formula can be viewed in Appendix B.

$$\rho_2 = \frac{(\frac{m_{empty,2}}{m_{empty,1}})*(\rho_1 * V_{full,1} + m_{empty,1}) - m_{empty,2}}{V_{full,2}} \quad [3]$$

In this equation, the Greek letter roe, ρ, represents the density of the fluid, m represents mass, and V represents fluid volume. Anything denoted with full means that this is the value found when the vessel is full of fluid, and anything denoted empty means that it is the value found when the vessel is empty. Additionally, anything denoted with a 1 is for the larger vessel and anything denoted with a 2 is for the 18-inch model.

This pressure vessel geometry has a "worst case scenario" when the manway is facing in the direction of the flow path. The manway causes a change in the center of gravity as it is the only thing causing asymmetry among the entire body. Due to this non-uniform geometry, the center of gravity of the pressure vessel is shifted in the direction of the manway, not in the middle of the vessel. In normal operation with no dynamic interference, gravity is pulling the vessel slightly in the direction of the vessel, but the structure can manage this imbalanced weight. It is not until the force of gravity is met with the added dynamic loading of wind that the vessel begins to fall. This worst-case scenario is the basis for the experimentation: the pressure vessel will not fall unless it is aligned in this worst-case scenario when exposed to a wind speed that is near its toppling wind speed. If the dimensional vessel is to topple, then this means that the loadcells on the same size of the manway are going to withstand a greater loading than the one opposite to the manway. An illustration of this worst-case scenario is shown in figure 1.13 below.

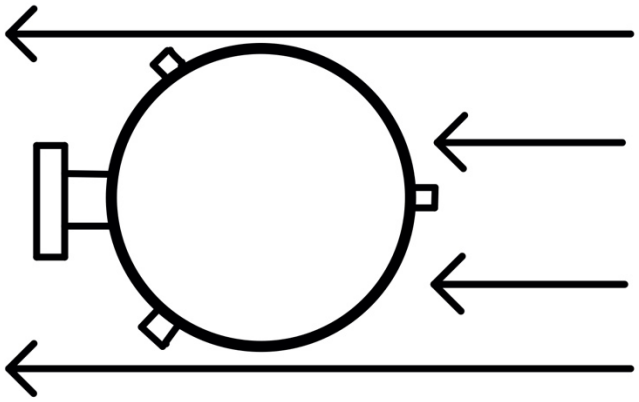

Figure 1.13: Worst Case Scenario Illustration

Another piece of testing equipment that is being used is a camera. The camera is used to record the tests as they are being performed to have a record of the tests being completed. For this testing, the specific camera being used is a Sony A6000 camera with a 24mm Rokinon prime lens. These videos were shot in an XAVC S file format to allow for slow motion capturing. The videos were recorded in 60p 50M. This means they were high quality videos captured in an aspect ratio of 1920x1080 pixels with a bit rate of 50 Mbps. The frame rate of the footage is captured in 1/125 seconds, allowing for slow motion capturing to be possible. A tripod is used to steady the camera and ensure that it captures the important parts of the tests.

This experimental setup works because it proves that a directional flow of wind over a similar cross section of wind will cause an imbalanced loading over the legs. If the wind is able to push over the scaled-down vessels, it proves that a larger magnitude wind, such as that in a hurricane, can cause an imbalanced loading on the loadcell structures. If such an imbalance can be proven to exist, then the source of an added loading can be determined, and a conclusion can be made about the strength of loadcells being used to support pressure vessels. In order to prove and definitively find an experimental value for

toppling, this experiment was conducted three times per weight and volume condition. The pressure vessel models will go through three different speeds from the wind tunnel: a speed where toppling is not likely, a speed where toppling is possible but not definite, and a speed where the model should always topple. For example, the 200 Cuft model will be tested three times with no fluid inside of it. The deliverables for this experimentation are to prove experimentally that a scaled-down realistic model will topple in a proportionate wind when it hits a certain wind speed.

1.4 SURFACE IMAGING FUNDAMENTALS

These pressure vessels rest on three legs, and each leg has a load cell attached. The loadcells have the primary purpose of measuring the weight of the pressure vessel using carefully placed strain gauges. As the loadcell is the initial point of failure for the body as a whole, it is needed to determine the type of fracture that occurred to fully understand if the loadcell was affected by an impact load or was worn down due to fatigue. In order to determine the type of failure, surface imaging techniques are employed. Surface imaging is a form of non-destructive testing that uses a very finely calibrated microscope to analyze the fracture surfaces or surface cracks of a body. Georgia Southern University has a Keyence VHX-1000 surface imaging microscope with a VH-Z20R and a VH-Z500R lens. This is an advanced piece of equipment capable of taking stitched images of surfaces between 20X and 200X magnification. It also has the functionality to create 3D surface renderings of non-uniform surfaces. Specific information on the VHX-1000 microscope can be found in Keyence VHX-1000 catalog. Additionally, Keyence made available a VHX-7000 microscope with a comparable range

to the VHX-1000 on site. This VHX-7000 microscope was employed for some of the scans shown in this research.

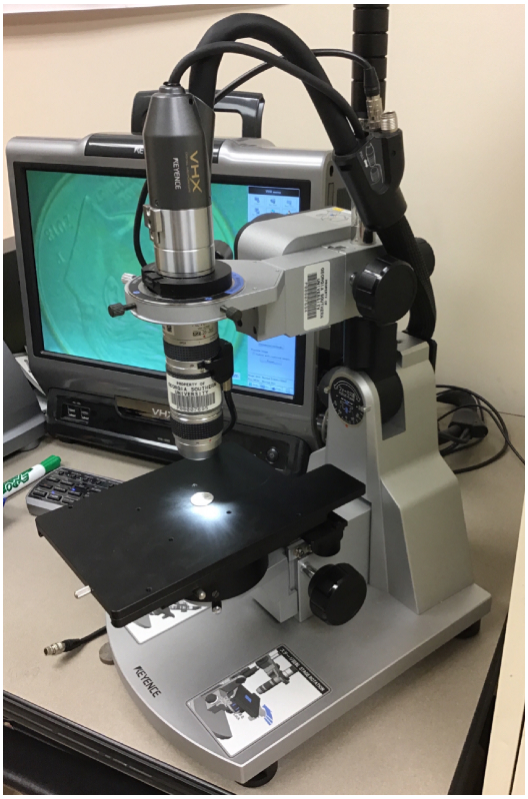

Figure 1.14: Keyence VHX-1000 Microscope system with VH-Z20R Lens

The loadcells are made out of 17-4 stainless steel, also known as SAE Type 630. According to Matweb, 17-4 stainless steel is a martensitic alloy of stainless steel that has very good strength up to 600ºF and good corrosion resistance. (Matweb 2020) It is widely used in aerospace, petrochemical, food processing, chemical, paper, and general metalworking industries. Material Property information from the matweb and a report titled “Physical and Mechanical Properties of Cast 17-4 PH Stainless Steel” by H. J. Rack from Sandia National Laboratories can be seen below in table 1.4. These values are taken at room temperature, or 20ºC or 70ºF. The material density, yield strength, and ultimate

tensile strength properties are taken from matweb while the Young's modulus and poisons ratio are taken from data in the Rack report. (Rack 1881, 26) Also known as the point of no return, the yield strength is the point where the elastic zone ends with the material and the applied stress causes a plastic deformation. Elastic deformation is deformation that is recoverable by the geometry of the body, while plastic deformation is a permanent disfigurement of the body when placed under pressure. Ultimate yield strength is the amount of stress that the material will fracture at. The Youngs modulus is a measure of the stiffness of the bonds of a material (Askeland 2016, 219) and is found by finding the rate of change of the elastic region on a stress-strain curve. The Young's modulus of a material is used in calculations to measure the effects of a loading on a material. Different materials stand up to loading differently. Finally, the Poisson's ratio is a relationship between the longitudinal and lateral strain of a material undergoing stress.

Table 1.4: Material Properties of 17-4 Stainless Steel		
Property	SI	US Customary
Density	7,780 kg/m^3	0.281 lb/in^3
Youngs Modulus	204.8 MPa	29.7 ksi
Poisson's Ratio	0.290	
Tensile Yield Strength	1000 MPa	145 ksi
Ultimate Yield Strength	1103 MPa	160 ksi

Fatigue failure is a part of this testing that is going to be investigated. Fatigue failures are failures that happen due to dynamic oscillations that induce internal stresses to the body of a specimen. When a body is experiencing fatigue as a result of vibrations or repeated impacts, the stresses applied are generally sinusoidal. They are applied in different magnitudes over time and this wears down the strength of the material in a manner that will not be seen in a static failure. For this particular research, the fatigue loading is most likely applied as an irregular stress cycle, meaning that it is coming in random magnitudes over time and it is less predictable. This is due to the fact that wind does not happen at a constant rate. In operation, the pressure vessels seen here are not under a constant wind loading at all times of the day, but rather they experience wind loadings in different, more random magnitudes over time. Fatigue life has three phases when a body is beginning to show signs of wear as a result of fatigue. The first phase of fatigue failure is initialization. This is where the crack begins to form due to a cyclic plastic deformation. From this point on, internal stresses only continue to build. The second phase is where the specimen continues to crack slowly, and the internal stresses continue to grow. This is also where corrosion will begin to take a role in the crack propagation. If the crack is under a corrosive environment such as a very humid environment, the crack will continue to grow due to corrosion regardless of a dynamic loading. The final phase is the failure phase. Once the cracking in stage 2 grows wide enough, the body will crack and fail a lot faster. This is due to the material that is still attached not being sufficient to carry the loading that is being applied to it. It is important to mention that the crack only grows at a faster rate as the crack is initialized at phase 1.

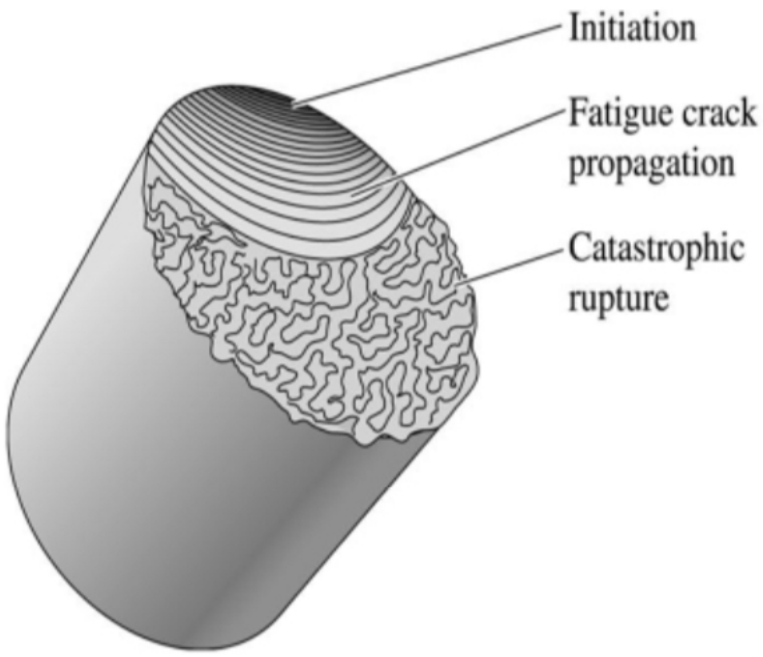

Figure 1.15: Graphic Showing General Fatigue Life (Askeland 2016, 246)

A static analysis of the loadcell geometry has been performed to understand the strength of the loadcells. These static analyses are performed using ANSYS software on the loadcell baseplate. ANSYS is an accurate engineering software used primarily to see how differing boundary conditions affect certain geometries and is used significantly throughout the engineering community. This particular static analysis shows the effects of the loadcell weight under the empty condition and the water-filled conditions. This static analysis shows the locations and the magnitudes of the internal stresses induced by the weight of the vessels. This means that the most likely failure point is going to be the point of highest stress and that the magnitude of stress induced by this force will be shown. Using a static structural simulation, the boundary conditions were set up with two fixed supports where the loadcell is simply supported and a force equivalent to 1/3 of the weight of the pressure vessels in each position as this represents the static loading of the

pressure vessel over the loadcells. A static environment is one where there is no dynamic loading present. Screenshots of the failure points for the geometries can be seen below in figures 1.16 and 1.17 to illustrate where a fracture would happen under a catastrophic loading. The magnitudes of the stresses caused by the static loading can be viewed below in table 1.5.

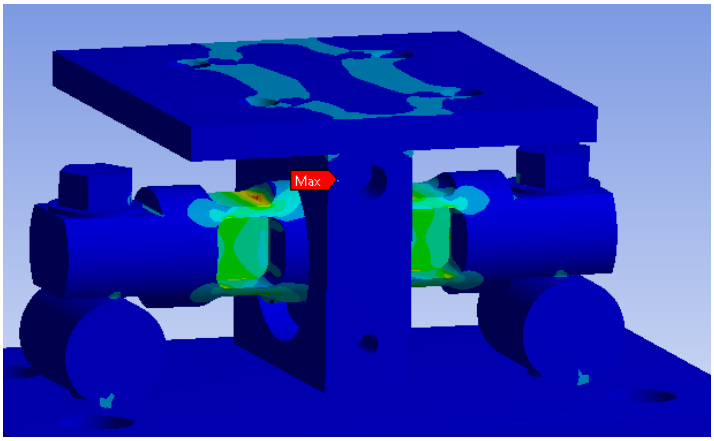

Figure 1.16: Static Analysis Results for 50 and 200 CUFT Loadcell

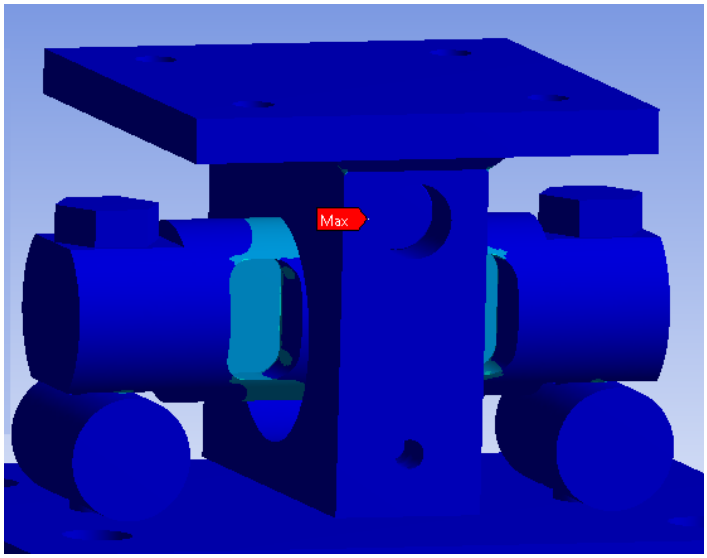

Figure 1.17: Static Analysis Results for 1100 CUFT Loadcell

Table 1.5: Static Analysis Maximum Equivalent Stresses			
	Empty Condition (MPa)	Catalyst-Filled (MPa)	Water-Filled Condition (MPa)
50 Cuft	36.8	109	132
200 Cuft	68.9	358	429
1100 Cuft	114.6	623	737

Based on this static analysis performed on the geometry in ANSYS, the loadcell will experience maximum stress at the internal side of the webbing of the load cell. This is considered the weakest part. It is important to note that these analyses show the point of highest stress when the load is applied, but it shows entirely static loading. When the dynamic factors, such as wind and seismic, are applied to this loading, it is subject to grow in magnitude and potentially fracture the structure. This provides a good preliminary analysis for the surface imaging test as it allows for the researcher to determine multiple points of concern before analyzing the loadcell itself.

When looking into this potential fatigue loading, there are two types of failures: ductile and brittle. A ductile break generally means that there is going to be some curvature to the break. The surfaces of the break are rough due to the longer nature of this type of fracture. Ductile fractures generally happen under a low impact, highly repetitive type of fatigue. Ductile fractures are the most common type of breaking within a metal. The other type of fracture is brittle. Brittle fractures are generally caused by high magnitude impacts on the fracturing body. When looking for a brittle fracture, there is generally a smooth surface on the fracturing face where the body sheared altogether,

rather than peeling apart over time like seen in ductile fractures. These are most common in ceramic materials but are not uncommon in metals if the conditions are right. For example, when analyzing fractures on different metal materials like stainless steel, a brittle fracture could be possible and are generally very easy to detect. Before most brittle fractures occur, the fracturing face is generally weakened and surface cracks begin to form, causing an internal stress anomaly to be formed around the face of the cracks. From the point surface cracks are formed, a brittle failure is common after a large load adds to the already-taxing internal stress caused by the surface cracks. The body generally gives quickly under a force that is too much for it.

When performing 3D scans with the Keyence VHX-1000 microscope, there are a few major points that should be considered that could impact the quality of scan. As the VHX-1000 did not have a built-in axial motor to automatically move the lens for the scans, the specimen must be moved manually. While the VHX-1000 has state-of-the-art tracking technology allowing it to stich images together, it can lose its location if the specimen is moved too drastically. It is important to pay very close attention to the scan that is being performed to ensure that the microscope does not lose its frame. Another major consideration is ghost depth. Ghost depth is a phenomenon that happens only during 3D scans where the microscope is unable to clearly read the depth that is present. This is generally because the upper and lower limits simply do not encompass the area and the microscope is needing to fill its perceived void with something OR the brightness of the microscope is too high and the light is reflecting back into the lens at a high magnitude, causing it to provide inaccurate readings. Ghost depth generally looks like mountains; it looks as if the computer generated an area of higher depth that is not

apparent, and it is viewed easily when looking at the final scan. If the ghost depth in the scan is caused by the microscope simply not having the area in its scanning range, the area scans will still be accurate, but the scale may be thrown off. The only fix to this to view accurate results after this type of ghost depth is to change the scale range. If the ghost depth is caused by too much reflectivity, the best course of action is to re-perform the scan. An example of ghost depth can be seen below in figure 1.18. There is not a method for altering the physical depth when post processing using the Keyence software available at the time of the VHX-1000. The VHX-7000 is more advanced and this issue is not generally seen with it.

Figure 1.18: Example of Ghost Depth taken on the VHX-1000

The ghost depth shown above is taken on the contact region between the loadcell and the loadcell bracket; this section is discussed later in section 3.2.3. There is no large depth in the middle of this specimen, but the image scan did not accurately complete that scan and it placed this depth in this spot.

While surface imaging will provide a strong basis for analyzing the failure modes of these loadcells in this configuration, there is also a need to quantify the depth of the crack in a manner that is repeatable. Surface imaging techniques can analyze some level of depth into small cracks and complex geometry, but there are more possible means for providing an on-the-spot analysis of the state of a loadcell and the depth of the crack. A way to do this is to perform a potential drop test. Potential drop tests are a form of non-destructive testing that send a constant electric current over a cracked or fatigued surface from one electrode to another to measure the electrical resistance or impedance of that crack. The theory of that is that the electrical current will move around the crack and generate a higher potential drop, or resistance, as it moves from electrode A to electrode B. There are two main types of potential drop tests performed: the DCPD, or DC potential drop, and the ACPD, or AC potential drop. The DCPD uses a high magnitude, usually 30 A, to send electricity over the crack while the ACPD uses a low magnitude, usually 1 A, to send electricity over the crack. ACPD tests are confined to surface cracks as there is a phenomenon called skin effect. The skin effect is when AC current travels over the surface and does not penetrate well the body of the test subject due to the nature of AC current and the magnitude of this current. DCPD is not subject to the skin effect, which makes it ideal for testing deep cracks especially in ferromagnetic materials such as stainless steel. Both of these potential drop techniques are used extensively in the field of fatigue testing and can provide accurate sizing for cracks. They are used also in crack sizing and detection for welds in the industry. A DC method for testing this particular crack may be best to avoid the skin effect that comes with AC current, but, as DC methods require a larger current value to “improve the signal-to-noise ratio,” (Corcoran

2020, 1), the effects of joule heating are often noticed. Joule heating, or resistance heating, is a phenomenon where sending an electric current through a material causes a heat to be dissipated by the material. A quasi-DC signal is a low-frequency signal (generally 0.3 Hz to 30 Hz) that is generated with a low amperage (10 mA to 40 mA) value. Methods for measuring crack creep in stainless steel can be created based on these quasi-DC principles but will need to be modified for the application of this loadcell.

In this experiment, the goal is to find any clues that the fractured surface may give away as far as how the loadcell fractured. This will provide a greater understanding to the type of weigh the loadcells take under the pressure vessels and under dynamic loadings. Two loadcells were provided for the purpose of this experiment: one fractured completely and the other unfractured but showing surface cracks. For this report, the fractured loadcell will be referred to as “fractured” and the unfractured load cell with surface cracks will be referred to as “unfractured.” The two can be seen side to side below in figure 1.19; the fractured loadcell is on the bottom and the unfractured loadcell is pictured on top.

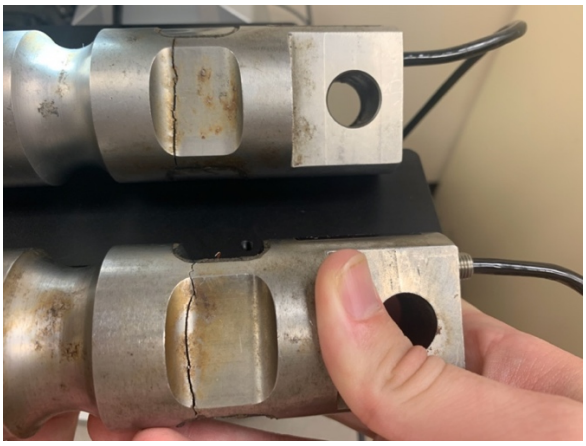

Figure 1.19: Fractured and Unfractured Loadcell Side-By-Side. The unfractured loadcell is depicted above the fractured loadcell

2. METHODS

2.1 WIND EXPERIMENTATION

The first step in this experiment is to prepare the models. 18-inch models were theorized using a dimensional analysis and the models were generated using Solidworks. After creating the CAD model, the file was converted to an STL file and the models were 3D printed using ABS plastic. The model had to have been printed in multiple parts, so an adhesive was used to piece the parts together. Once the model is created, the abs plastic is quite porous. In order to combat the effects of porosity in the plastic, a rubber sealant coating was used to add a protective layer to the vessel. This process was performed for the 50 Cuft, 200 Cuft, and 1100 Cuft vessels. Once these steps were completed, the vessels were ready for testing.

After preparing the vessels, the experiment must be set up. Georgia Southern University's subsonic wind tunnel was used to provide the steady wind loading required for this experiment. The testing surface consists of a smooth steel plate to be used as a ground surface to lay the pressure vessel models. This steel surface was marked out at 3" intervals. The testing surface is also enclosed by thin sheets of aluminum placed at a sufficient distance so that the boundary layer does not affect the flow of air around the pressure vessel. The wind tunnel was energized and began to produce wind. The pressure vessel models were put in the wind flow path and the frequency of the fan generating wind was increased and decreased until the desired conditions were met for the test that was being performed. The desired conditions for the test being performed are based on the theoretical dimensional analysis toppling values. Once the frequency had been found, Omega anemometers were used to measure the wind speed every testing location, every

six inches, on the steel plate. A rubber sealant coating was used to decrease porosity in the models and ensure that the experiment was going to be accurate. Figure 2.1 below shows the testing platform. The blue at the top of the picture is the end of the wind tunnel which directly flows into the testing area. The black sharpie lines are the three-inch intervals that are measuring where the vessel will be placed.

Figure 2.1: Testing Platform for Wind Loading

With the models ready and the wind tunnel set up, the experiment can be performed. A camera was set up to document all testing. Once this is completed, the test can be performed. Very carefully, the 18-inch models were placed in 6 different orientations at every 6-inch testing location of the steel plate. The positions started with the manway facing into the wind tunnel, then it was oriented 60º until it had completed its rotations. The third orientation is the worst-case scenario where the manway was in the

same direction of flow coming out of the wind tunnel. The model was allowed to sit in the flow for roughly 30-45 seconds until it was either confirmed that it toppled or did not. This process was repeated until all locations on the steel plate had been tested. The speed values at each point and the result of the test were recorded for further analysis. This experiment is completed for all weight conditions, including empty and catalyst-filled, and all volumes, including 50 Cuft, 200 Cuft, and 1100 Cuft.

In setting up the catalyst-filled tests, a food processor was then used to atomize activated carbon and Styrofoam so that this mixture can be created. The pressure vessel models are then filled with Styrofoam, as it is the least dense of the materials and it fills more space until the vessel was roughly ¾ full. Then the powdered carbon was added to fill the rest of the volume and achieve the scaled-down mass related to the . This allows for the catalyst substitute to be added without changing the level at which the weight changes the center of gravity of the pressure vessel.

From these results, the experimental toppling wind speed can be determined. This experimental toppling value is then compared to the theoretical toppling value that was calculated prior to experimentation.

2.2 SURFACE IMAGING

In order to analyze the fracture on the loadcell to determine its nature, the following equipment was used. Georgia Southern University owns a Keyence VHX-1000 microscope with a VH-Z20R and a VH-Z500R lens. The first step in ensuring this microscope is ready to analyze is to ensure its configuration. The white balance hue was reconfigured every time the microscope was used to ensure the coloring was accurate. To do this, the microscope lens was moved 25.5 mm away from the viewing surface and a

white surface was inserted in the entirety of the microscope view. Using the hand controller shown in figure 2.2 below, the “white balance” option was selected. The microscope then automatically adjusts its white balance hue to that page. For scans completed using the VHX-7000 microscope, the same photo preparation techniques were used but the VHX-7000 is a lot better at dealing with ghost depth and taking a complete picture. It also has built in motors to the base so it is hands free after setting the photo path and scan depth.

Figure 2.2: Hand Controller for VHX-1000 Microscope

After the software configurations are set up and verified correct, the loadcell and microscope must be prepared for the scan that is being performed. There are multiple scans being performed to completely analyze the loadcell. For the sake of repeatability, all scans that are applicable to both the fractured and unfractured loadcell will be performed on both with the same magnification and settings.

The first scans to be performed were 2D scans of the broken faces of the fractured cell. In order to prepare this scan, a wire brush was taken lightly to the surface to rid it of any obvious sediment or burrs on the surface. Due to the length of the loadcell, the face

cannot fit properly under the lens of the microscope without some modifications. In order to account for this, the loadcell bodies were laid flat on the testing center and secured in place and the microscope arm was rotated 90º so that the face of the lens was completely parallel with the loadcell face. This orientation can be seen in figure 2.3. This is due to the loadcell specimen being too large and awkwardly shaped to fit under the microscope itself.

Figure 2.3: 90º Orientation of Microscope

The microscope body must be moved higher up on the arm to ensure that there is a free range of motion throughout the entire fractured face. Once it is confirmed that the entire lens can capture the face of the loadcell without moving or manipulating the distance between the lens or without moving the loadcell itself so as to not mess up the focus on the shot, the 2D image stitch of the face is ready to be created. The first step in preparing all of the image stiches is to ensure the magnification, focus, and brightness are ideal. For

the first scan, the magnification was set to 20X and the lens was focused on the middle point of the face. The brightness was then set so that the surface could be seen but was not too shiny. The 2D image stitching was started following this and the face of the fractured loadcell was moved around until it had been captured in its entirety by the lens. This 2D scan was repeated for the other end of the loadcell as well and all necessary points were documented.

A 3D scan was then completed using the same configuration as the 2D scan to view the depth of the loadcell and create a profile of each face. With the arm still at 90º and the lens face still parallel to the face, the magnification and brightness were set. The magnification was set to 30X as that provided a good view of the loadcell face without attempting to scan too much outside of the fractured face. A general best practice with the 3D scans is to scan the surface that is in question and attempt to get as little of the outer surface in the frame as possible as the outside is generally poorly lit and not focused by the lens, causing errors in the views. It is imperative when running the 3D depth scan of a material as reflective as stainless steel that the brightness is not too high. A brightness that is too high can lead to errors in the depth perception of the lens as the light being reflected could give the machine a perceived depth that is not present in the actual geometry. The brightness for these scans were set relatively low at roughly 30% of the maximum brightness. These settings are configured before hitting the 3D stitching option. Once they are finished, the 3D stitching option was opened. The 3D stitching options are then opened and reviewed. Firstly, the lens and magnification must be selected in the settings here to ensure that the depth scan is going to be calibrated correctly. For these scans, the Z20 lens and 30X magnification were selected. Following

this, a ‘low limit to up limit’ boundary was set. In order to set the up and low limits, the testing base with the loadcell on it was manipulated so that the highest and lowest parts were showing respectively. Then, the sweeping feature in the microscope was used to move to where the most extreme points were in focus by the microscope. The bounds are set at the points where the most extreme points in the geometry are in focus. The images are now ready to be taken. The image capturing was initiated and the fractured face of the loadcell was moved around so that there was an image captured at each point. The microscope takes about 20 seconds to sweep from the lower limit to the upper limit and stitch all of the images together. Once the scans were complete, the 3D depth model of the face could be analyzed. In order to create the profile, two points of interest were identified within the program and the .CSV file containing the depth values between those points were created. For the profiles found in this report, the points of interest were on opposite ends of the loadcell through the vertical web, traveling directly through the center of the cut. Figure 2.4 provides an idea of how the loadcell faces were oriented with the microscope

Figure 2.4: Loadcell Face Being Scanned By Microscope

Next, the contact surface between the top pin in the loadcell bracket and the loadcells need to have a 3D depth scan performed to determine if the added loading is transferred from the pressure vessel to the loadcell via rubbing or via small impacts. For this test, scans at two different angles were performed. Both tests had the same settings, however. The first scan was performed with the arm at no angle; the upright position for the microscope. This allowed for a straight down shot onto the loadcell. The second test was performed at a 10º angle from the upright position. This put the lens normal to the obvious markings of the loadcell. This scan was performed on both of the loadcells: fractured and unfractured. Before this test was performed, a wire brush was used to prepare the surface and clean it of some dirt that was present prior to testing. There were small patches of sediment on both loadcells. After getting rid of those, the loadcell was fixed into the testing center and positioned to where the microscope could view it. The

brightness and magnification are the first two things to determine. The magnification was set to 30X. This section of the loadcell is significantly shinier than the previous test, therefore the brightness was turned down to preserve accurate results and not allow for ghost depth. The 3D image stitching feature was then booted up. The upper limits and lower limits were found based on the highest and lowest points in the testing area and the scans were performed as described in the previous paragraph. This test was repeated two times: one for each loadcell. The profiles were then viewed and compared to ensure it was the same type of mechanism applied to each of the loadcells.

The unfractured loadcell also had a large surface crack on the bottom side of it. A scan should be created from this to attempt to see how deep it is and to view the profile of it as the profile may provide clues to what the exact spot that broke first was. In order to perform this scan, the microscope arm was upright entirely. The magnification was set to 30X and the brightness was set roughly to 40% of its capacity in order to get a good view into the fracture while not allowing the light to show ghost depth in the results. The scan was performed, and the pictures were taken along the surface of the crack. The results were then analyzed and compared to the fractured surface of the fractured loadcell.

3. DATA – RESULTS - ANALYSIS

3.1 WIND EXPERIMENTATION

When starting this experiment, the first step is to find the wind speeds at all marked locations. The below tables, tables 3.1, 3.2, and 3.3, show the average wind speeds for all tests at six-inch long intervals for the empty pressure vessel tests and the result of exposing the pressure vessel model to this wind speed. If the value in the fail column is a "Y," this means that the pressure vessel model experienced failure under this wind speed and if the value is "N," this means the pressure vessel model was stable throughout that wind speed. All speeds below are documented in miles per hour. These values are taken with the same Omega anemometer so as to preserve consistency.

Table 3.1: Empty 50 Cuft Testing Results

#	Distance (Inches)	No Failing Wind Speed (mph)	Fail?	Might Fail/Toppling Wind Speed (mph)	Fail?	Definite Failure Wind Speed (mph)	Fail?
1	6	6.8	N	7.0	Y	7.4	Y
2	12	6.7	N	6.9	N	7.1	Y
3	18	6.6	N	6.8	Y	7.0	Y
4	24	6.6	N	6.8	Y	7.0	Y
5	30	6.5	N	6.8	Y	6.9	Y
6	36	6.7	N	6.8	Y	6.9	Y

Table 3.2: Empty 200 Cuft Testing Results							
#	Distance (Inches)	No Failing Wind Speed (mph)	Fail?	Might Fail/Toppling Wind Speed (mph)	Fail?	Definite Failure Wind Speed (mph)	Fail?
1	6	7.1	N	7.9	Y	8.2	Y
2	12	7.0	N	7.8	N	8.2	Y
3	18	7.0	N	7.8	Y	7.9	Y
4	24	7.0	N	7.7	Y	7.9	Y
5	30	6.9	N	7.6	N	7.7	Y
6	36	6.8	N	7.4	N	7.7	Y

Table 3.3: Empty 1100 Cuft Testing Results							
#	Distance (Inches)	No Fail Wind Speed (mph)	Fail?	Might Fail Wind Speed (mph)	Fail?	Definite Failure Wind Speed (mph)	Fail?
1	6	9.22	N	9.31	Y	9.69	Y
2	12	9.15	N	9.22	Y	9.51	Y
3	18	9.10	N	9.10	Y	9.40	Y
4	24	9.06	N	9.06	Y	9.31	Y
5	30	9.01	N	9.06	Y	9.26	Y
6	36	8.88	N	8.92	N	9.15	Y

In solving equation 3 above, the perfect substance to replace the density is a mixture of powdered carbon and Styrofoam. Powdered carbon has a density of 80 kg/m^3 and Styrofoam has a density of 50 kg/m^3. An interpolation of these materials was performed to discover a volume of each that needed to be added to each vessel in order to simulate the catalyst-filled conditions. A sample calculation is provided below using equation 3 and equation 8 in appendix B to find the density and mass for the 200 Cuft pressure vessel model. Table 3.4 shows the required density to fill the volume of the vessel and the mass of the fluid required to fill this volume based on the density below.

$$\rho_{200\,Cuft} = \frac{\left(\frac{m_{empty,2}}{m_{empty,1}}\right) * \left(\rho_1 * V_{full,1} + m_{empty,1}\right) - m_{empty,2}}{V_{full,2}}$$

$$= \frac{\left(\frac{0.171\ kg}{4252.9\ kg}\right) * \left(878.2\ \frac{kg}{m^3} * 6.51\ m^3 + 4252.9\ kg\right) - 0.171 kg}{0.003\ m^3}$$

$$= 74.8\ \frac{kg}{m^3}$$

$$m_{200\,Cuft} = \rho_{200\,Cuft} * V_{200\,Cuft\,Model} = 74.8\ \frac{kg}{m^3} * 0.003\ m^3 = 229.2\ g$$

Table 3.4: Required Experimentation Densities for Each Pressure Vessel Model

Pressure Vessel	50 Cuft	200 Cuft	1100 Cuft
Required Density (kg/m^3)	71.3	74.8	119.2
Required Mass (g)	122.1	229.2	434.5

The catalyst-filled pressure vessel tests were now run. These tests were also run with the catalyst-filled condition as that is the condition the pressure vessel was generally in. After filling the 18-inch models with the catalyst replacement**,** the tests were re-run.

Below are the wind speed values for the catalyst-filled simulated tests in tables 3.5, 3.6, an 3.7 for the 50 Cuft, 200 Cuft, and 1100 Cuft.

Table 3.5: Catalyst-Filled 50 Cuft Testing Results

#	Distance (Inches)	No Fail Wind Speed (mph)	Fail?	Might Fail Wind Speed (mph)	Fail?	Definite Failure Wind Speed (mph)	Fail?
1	6	9.31	N	9.51	Y	10.03	Y
2	12	9.22	N	9.40	Y	9.93	Y
3	18	9.10	N	9.26	Y	9.93	Y
4	24	9.01	N	9.22	Y	9.93	Y
5	30	8.93	N	9.10	N	9.80	Y
6	36	8.72	N	9.10	N	9.74	Y

Table 3.6: Catalyst-Filled 200 Cuft Testing Results							
#	Distance (Inches)	No Failing Wind Speed (mph)	Fail?	Might Fail/Toppling Wind Speed (mph)	Fail?	Definite Failure Wind Speed (mph)	Fail?
1	6	10.36	N	10.67	Y	11.27	Y
2	12	10.27	N	10.63	Y	11.23	Y
3	18	10.18	N	10.60	Y	11.23	Y
4	24	10.18	N	10.51	Y	11.18	Y
5	30	10.09	N	10.36	Y	11.10	Y
6	36	9.89	N	10.27	Y	10.98	Y

Table 3.7: Catalyst-Filled 1100 Cuft Testing Results							
#	Distance (Inches)	No Failing Wind Speed (mph)	Fail?	Might Fail Wind Speed (mph)	Fail?	Definite Failure Wind Speed (mph)	Fail?
1	6	11.29	N	12.17	Y	13.71	Y
2	12	11.18	N	11.97	Y	13.62	Y
3	18	11.09	N	11.83	Y	13.42	Y
4	24	10.94	N	11.68	N	13.33	Y
5	30	10.89	N	11.68	N	13.18	Y
6	36	10.84	N	11.50	N	13.00	Y

After reviewing these tests, experimental toppling wind speeds can be found for each model in each condition and can be compared to the theoretically calculated values found in Appendix A. In order to find the theoretical values, the mass divided by 3 values from table 3.8 are used to find the wind speed values that correspond to that particular loading. Table 5.2 holds the wind speed and applied loading relationships. The value that matches the mass divided by 3 value in table 3.8 for the respective pressure vessel sizing is the theoretical toppling speed. The following tables 3.9, 3.10, and 3.11 show the experimental toppling wind speeds, the theoretical toppling wind speeds, and the percent error respectively.

	Table 3.8: Weight Values to Find Theoretical Toppling Wind Speed			
		50 Cuft (lbm)	200 Cuft (lbm)	1100 Cuft (lbm)
Empty Condition	Mass	0.360	0.376	0.507
	Mass/3	0.120	0.125	0.169
Catalyst-Filled	Mass	0.629	0.881	1.465
	Mass/3	0.210	0.294	0.488

Table 3.9: Experimental Toppling Wind Speeds for Different Testing Conditions in Models			
	50 Cuft (mph)	200 Cuft (mph)	1100 Cuft (mph)
Empty Condition	6.8	7.85	9.06
Catalyst-Filled	9.22	11.05	13.91

Table 3.10: Theoretical Toppling Wind Speeds for Different Testing Conditions in Models			
	50 Cuft (mph)	200 Cuft (mph)	1100 Cuft (mph)
Empty Condition	6.6	6.8	7.4
Catalyst-Filled	8.6	10.4	11.8

Table 3.11: Percent Errors for Tests in Models			
	50 Cuft	200 Cuft	1100 Cuft
Empty Condition	3.03%	15.44%	22.43%
Catalyst-Filled	7.21%	6.25%	4.6%

After reviewing the results, it is determined that the experimental errors are all acceptable for the objectives of this project. With the experimental wind velocity values showing toppling within the loadcell models at wind speeds that are within a reasonable margin from the theoretical values, the theoretical values can be accepted. Using table 5.1 in Appendix A for wind speeds for toppling for the larger pressure vessels, the wind speeds at which toppling should be seen can be confirmed and are shown below in table 3.12.

Table 3.12: Theoretical Toppling Wind Speeds for Different Operating Conditions in Pressure Vessels			
	50 Cuft (mph)	200 Cuft (mph)	1100 Cuft (mph)
Empty Condition	71.6	83.3	88.0
Catalyst-Filled	89.7	126.6	146.7

It is very important to note that during this testing, the 50 Cuft and 200 Cuft pressure vessel models never showed signs of toppling in any position other than in the worst-case position. The 1100 Cuft did however notice shaking during the absolute failure test in positions that were not worst-case. This is probably due to the size of the manway in proportion to the pressure vessel body. The 50 Cuft and 200 Cuft pressure vessels have manways that are larger proportionally to their bodies where the 1100 Cuft, while its manway may be the same size in real life, has a smaller ratio of manway size to pressure vessel body size. This would cause the 1100 Cuft model to be more likely to experience shaking outside of the worst-case scenario.

3.2 SURFACE IMAGING

3.2.1 FRACTURED LOADCELL FACE

The first faces that were analyzed were the fracture faces on the broken loadcell using both 2D and 3D methods. Figures 3.1 and 3.2 show birds-eye 2D views of the concave and convex fracture faces respectively.

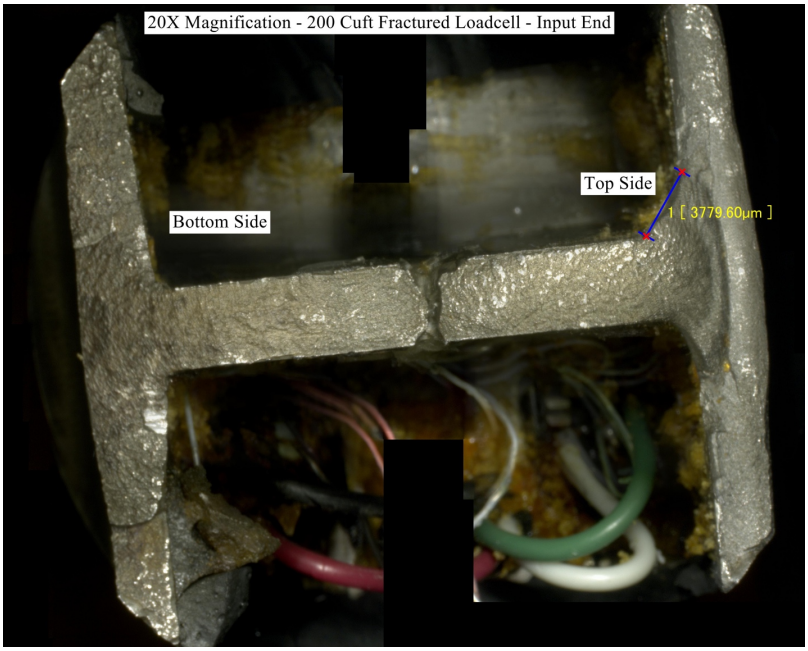

Figure 3.1: Convex Fractured Face, 2D Image Stitch at 20X Magnification

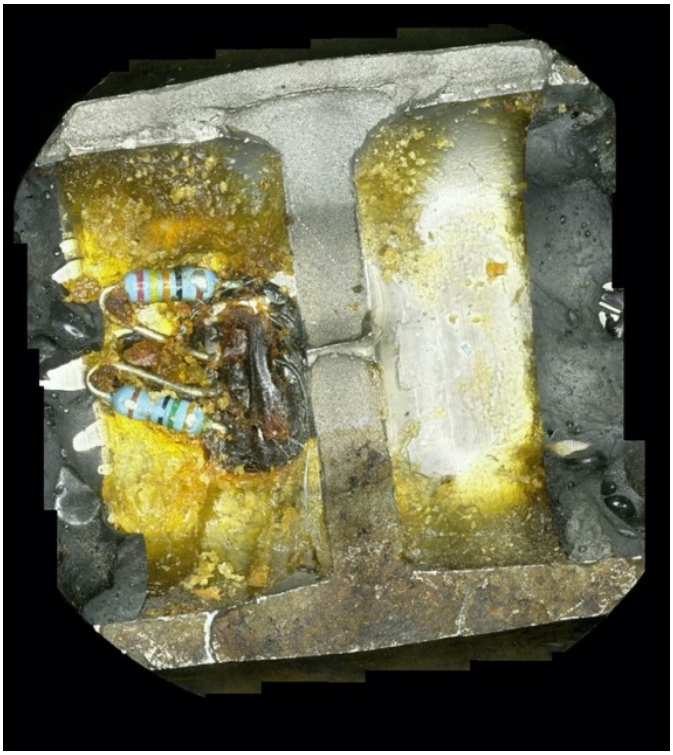

Figure 3.2: Concave Fracture Face, 2D Image Stitch at 30X magnification

A visual inspection of both of these images side by side shows that there is a discoloration between the two sides. This is especially apparent in figure 3.2 showing the concave fracture face. In figure 3.1, the top of the loadcell is towards the left and the bottom is towards the right. The bottom is where surface cracking has been observed in the other loadcells used commercially in the same configuration as this one. This discoloration is most likely due to exposure to the elements. Another major takeaway from these scans is that the surface appears rough. The initial 2D scans shows no areas on either fracture face that cause concern to investigate this as a brittle failure due to the surface roughness being uniformly rough. These faces are explored more through a 3D scan. Figure 3.3 shows the convex and concave images side-by-side after the 3D scan is performed.

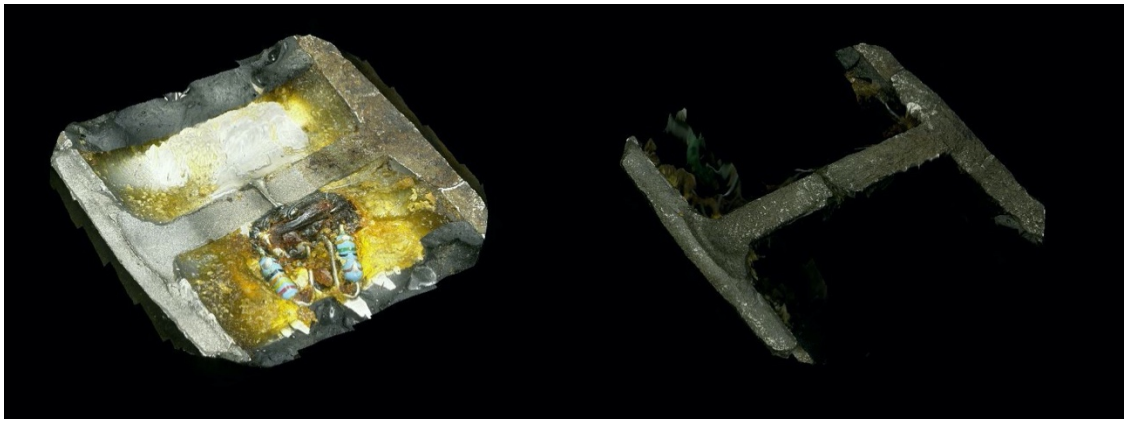

Figure 3.3: Concave Face (Left) and Convex Face(right), 3D Image Stitch at 30X Magnification

Immediately after reviewing these scans, the depth can be viewed in each of the faces and the conclusions can be drawn about them. The fracture faces have a non-uniform depth and are rough throughout the face, supporting the theory that this is a ductile fracture. Utilizing the results from the depth scan, cross-sectional profiles of the

fractured faces were created and are displayed in figures 3.4 and 3.5 for the convex and concave faces respectivly. These profiles display the curvature of both faces along the center of the fracture. The curvature goes from top to bottom of the loadcell moving left to right. It is important to note that these profiles show depth, therefore the lower the line appears in this graph, the farther away from the lens that spot was when the 3D scans were being performed. The center of the graph is obvious in this profile and it is likely more stretched out because it consists of a material closer to epoxy. Towards the left of these profiles are the final point of resistance for the material. Where the profile goes from straighter to increased concavity is the section where the web of the cross-section ends and the internal steel begins.

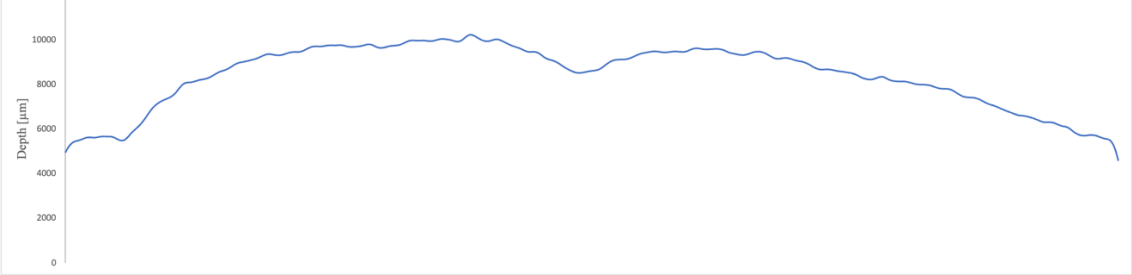

Figure 3.4: Profile of Convex-Face on the Fractured Loadcell

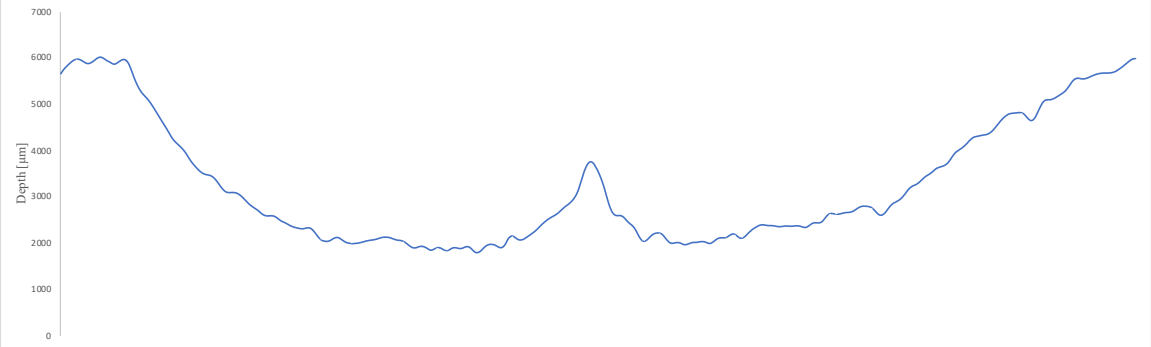

Figure 3.5: Profile of Concave-Face on the Fractured Loadcell

A point of interest for the fracture faces is the discoloration between the top and bottoms of the loadcell faces. Utilizing the measurement section feature after post processing the 3D depth scans, figure 3.6 was created. This figure shows that the discoloration starts 24.2 mm away from the top of the loadcell. This means that surface cracks penetrated the remaining 12 mm of material before a secondary fracture happened. The final important takeaway that can be conluded from these depth scans is about the color depth. 17-4 stainless steel has a good resistance to corrosion. These scans show that the surface has obviously seen some weathering, therfore a conslusion can be made that the loadcell was slowly cracking more and more.

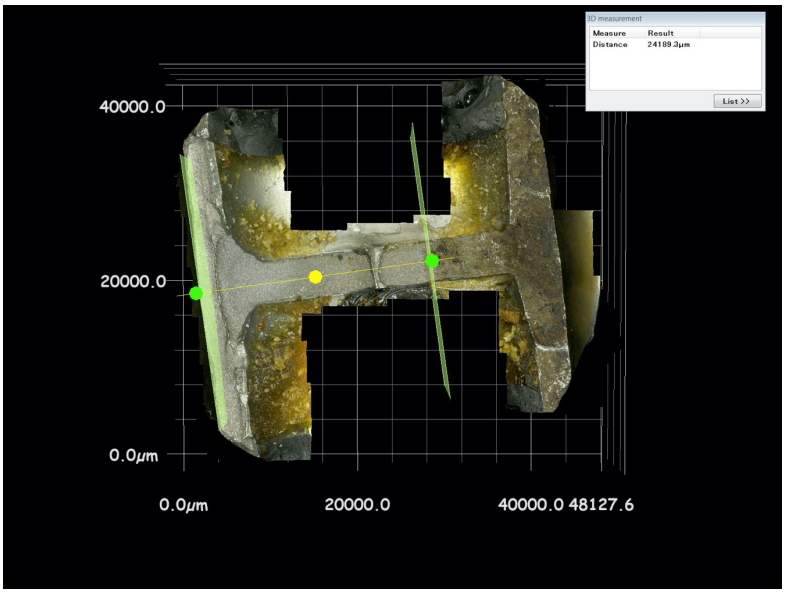

Figure 3.6: Discoloration Distance from Top of Fractured Loadcell

After performing surface imaging on the fractured loadcell face, very specific points are viewed that give particularly useful insight into how the loadcell fractured. Firstly, it is noted that the loadcell fractured on the inner webbing of the load cell, exactly where the static analysis computer simulations said the maximum stress would occur.

This confirms the legitimacy of the static analysis. Additionally, after reviewing the fracture profiles of the inner web of the load cell shown in figures 3.4 and 3.5, the fracture can be confirmed as ductile over brittle. Firstly, the profile through the major axis of this loadcell shows that the fractured surface is more of a concave-convex situation, meaning that the material peeled apart slowly from each other as opposed to a fast and brittle fracture. Additionally, the surface of the fracture is mostly bumpy and rough, which is associated with a ductile fracture as well. Reviewing the 2D scans of the fractured loadcell reveals also that there is a zone of discoloration. This is caused by a preliminary crack being formed with the surface cracks and creeping along the fractured plane slowly, until it reaches a specific point and the internal geometry of the load cell became too weak to hold the weight of the vessel, causing a secondary ductile fracture. This is shown by the discoloration of the loadcell fractured surface. The bottom third of the surface looks as though it has seen exposure to the elements, where the top half looks clean and free of any sign of oxidation. As the stainless-steel alloy of the loadcell is resistive to corrosion, the corrosion may not have had a drastic effect on the failure of the loadcell, but it definitely provides a good indication of the amount of time that the loadcell internals were exposed to moisture. This test of the face shows how the crack progressed over time given the fatigue loading. The crack initialization zone can be viewed via a previous zone, but phases two and three of the fatigue life for this loadcell can be seen clearly in the discolored sections. The darker zone is phase two, when the crack is growing due to corrosion and excess fatigue loadings and the cleaner, yet bumpy zone is where the catastrophic failure happened: it is where the material of the loadcell was no longer enough to support the weight of the pressure vessel.

Another branch of research for a deeper understand would be to chemically date the material around the fractures and figure out the amount of time the surface had been exposed to the elements. This would allow for a deeper understanding concerning the time frame it took the loadcell to crack under the impacts of the pressure vessel.

3.2.2 SURFACE CRACK

Now that the fractured face had been analyzed, the surface cracks on the unfractured loadcell were next up to view the similarities between the profile on the fractured loadcell and the unfractured loadcell and to attempt to identify a depth of the crack to see how far along in the process of fracturing this loadcell was. There are two cracks on this loadcell: one thick crack that spans the length of the loadcell and one smaller one that spans a small amount of distance on the other side of the center of the loadcell. Both of these cracks are on the bottom side of the loadcell; the opposite side to where the loading is applied. A side-by-side picture of the two loadcells can be seen in figure 1.19. The profiles of the fractures are of the same nature, and these close-up scans confirm the suspicions that these loadcells were impacted by the same type of loading.

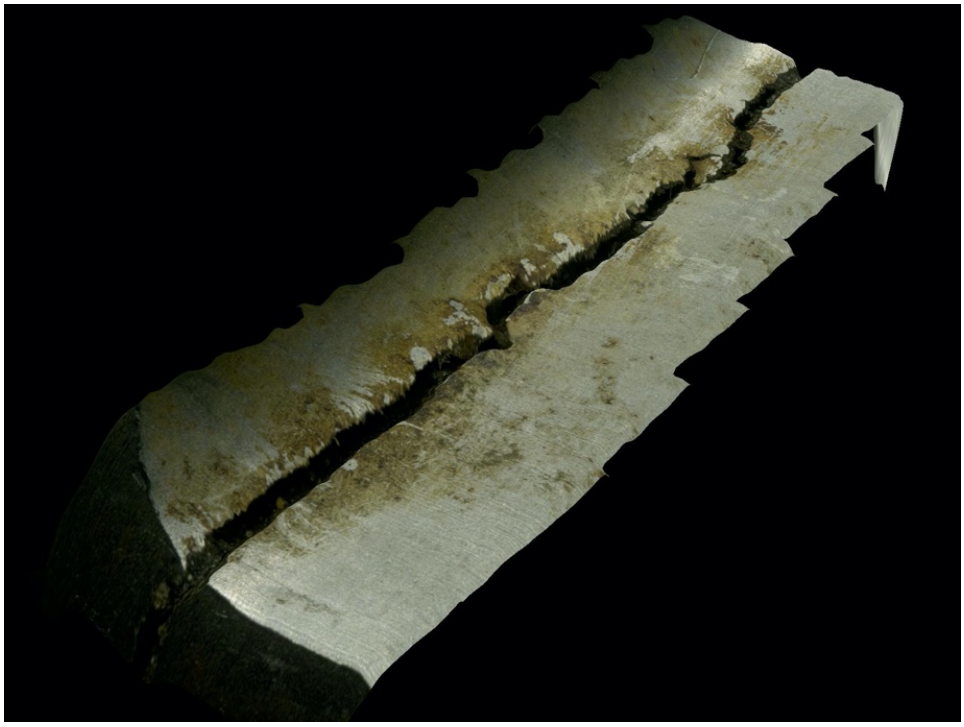

Figure 3.7: Surface Cracking on Unfractured Loadcell, 50X Magnification

This crack is coming off of a non-fractured loadcell but occurs in the exact same spot as the previously analyzed loadcells fracture, therefore the fractures are assumed to be similar in nature and origin. There are multiple important takeaways from this scan. Firstly, the depth of the scan is explored to see exactly how deep it is. Also, the width of the scan is analyzed to see exactly how spread apart the surfaces get and to confirm that it is wide enough to be exposed to the elements. In a humid environment such as the one these loadcells were operational in, it is very possible for a significant amount of moisture to infiltrate the crack profile. A top down view of the fracture without the measurement markups can be seen beside it in figure 3.8. Detailed results of this surface scan can be seen below in figure 3.9. It is observed that these profiles look very similar and have a few discernable features that could help locate a potential start to the cracking.

Figure 3.8: Top-Down Profile View of Loadcell Cracking, 50X Magnification

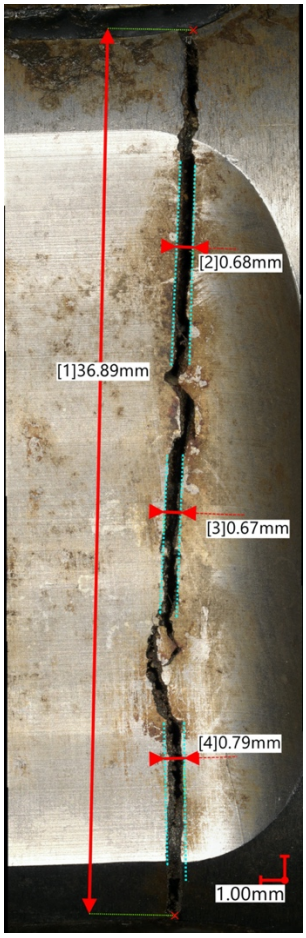

Figure 3.9: Detailed Top-Down View of Loadcell Cracking with Measurements, 50X Magnification

From figure 3.9, it can be seen that the crack is relatively uniformly wide, with a width of 0.67 mm at its skinniest and 0.79 mm at its widest. This is undoubtedly wide enough to allow moisture to penetrate the internals of the loadcell.

A profile of this crack was created to view the depth of it. This profile can be seen in figure 3.10 below. This depth was found using a single 3D scan of an area along the crack.

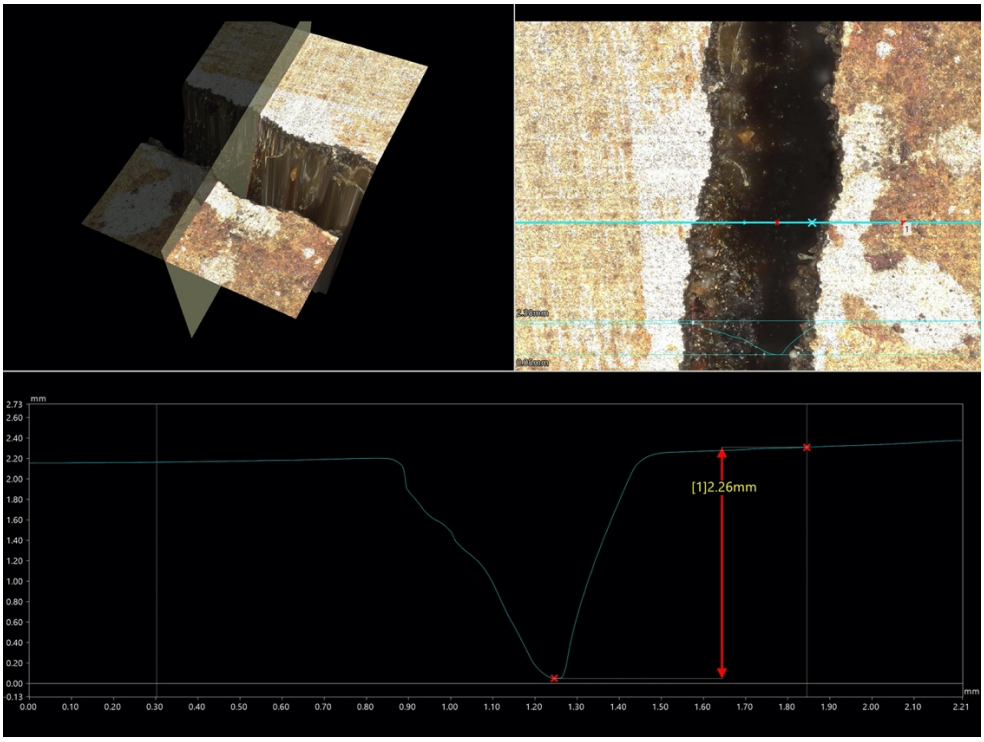

Figure 3.10: Depth Profile of Surface Crack, VHX-7000 80X Magnification

The deepest viewable point on the crack profile the microscope can view is 2.26 mm. This crack depth would only increase as forces continue to affect this loadcell. When compared to the fractured face of the previous loadcell, the first stage of the fracture showed roughly 12 mm of weathered depth, which means that the fracture could go deeper than is shown by the depth scan.

The next scan is the smaller one that looks as though it was just starting. A profile and distance were found from this crack and are shown below in figure 3.11. The most important takeaway from this smaller crack is viewing where the crack starts. This crack starts at the edge of the loadcell wall, which shows that the stresses are being applied at some sort of angle. This is also supported by the differentiation in the location of the impacts in the contact surface explored in the next section.

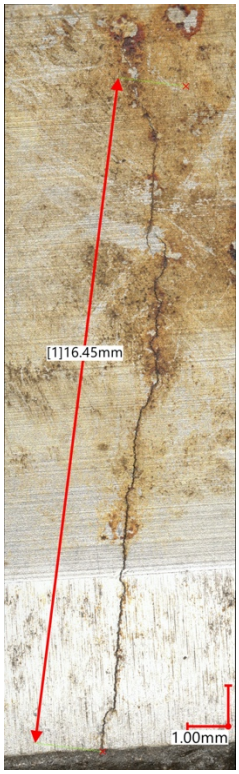

Figure 3.11: Small Surface Crack Profile, VHX-7000 30X Magnification

The width of this crack is not wide, and it is not very deep, it is the start of a crack. The presence of this crack, however, would cause stress singularities within the geometry and would definitely open up more if the loadcell were to continue to be used.

There is a lot to tell from these cracks to make some discoveries about the fractured loadcell. As it is of the same nature as the fractured loadcells profile, it can tell a lot of how the crack initialized. From the first surface crack, a clear depth is found, and it is quantified at least 2.26 mm deep. This wider crack is of the same nature as the 16.45 mm crack on the other side of the same loadcell. This is very important because it allows assumptions to be made about the starting location of these surface cracks and it allows for a view of the progression of these cracks. It is obvious after this analysis that the cracks start at one end of the load cell and works its way to the other as the internal

stresses compound on top of each other. This crack widens as it travels to the other side and becomes deeper, allowing for moisture and weathering to be introduced to the internals of the system. This test shows how the fatigue life is initiated.

A means of testing the real depth of these cracks can be developed as a future means to advance this research. A voltage drop test is currently being designed in conjunction with this report to quantify the depth of the surface cracks and potentially develop a non-destructive testing technique for finding surface cracks in loadcells that are in operation.

3.2.3 CONTACT REGION

The final location to perform surface imaging on is the contact zone between the loadcell and the bracket that connects it to the pressure vessel. This 3D depth scan was performed on both the fractured and unfractured loadcell, and on both there were signs of sediment buildup on the surface. After cleaning the surface with a fine wire brush, initial visual inspection concluded that there was an obvious sign of enforced contact between the top connecting pin in the loadcell bracket and the loadcell itself. Immediately, the contact zones prove the theory that the pressure vessel is adding weight to the loadcell under wind loading, but it is unclear as to what type of loading is being applied. Initial visual inspection led to two hypotheses as to how this force was being applied: the force is a rubbing force where the pin rubs the loadcell constantly or the force is a small-magnitude impact force caused by wind loading pushing the pressure vessel onto the loadcell. Additionally, visual inspection showed that the forces were not happening directly vertically downwards but rather slightly tilted. This is seen in figures 31 and 32 for the fractured and unfractured loadcells contact regions respectively. Specifically,

these figures show that the indentations are concentrated to one side rather than being directly in the center. In figure 3.12, the grouping of impact markings is shown to be concentrated towards the right side of the contact region rather than the middle of it. The same effect is seen in figure 3.13. Surface imaging helps make important determinations about the methods the forces were loaded. The VHX-1000 was used to take images of the unfractured loadcell and the VHX-7000 was used to take pictures of the fractured loadcell.

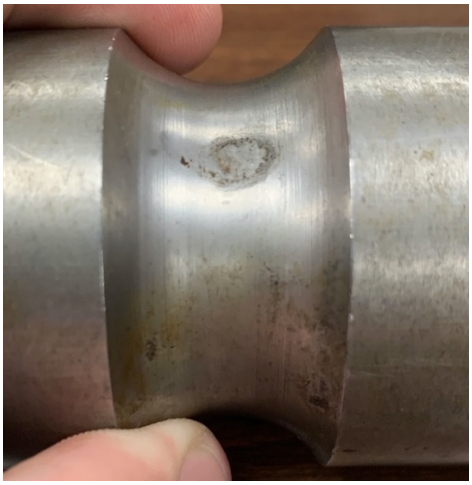

Figure 3.12: Fractured loadcell Top Down View Showing Non-Central loading

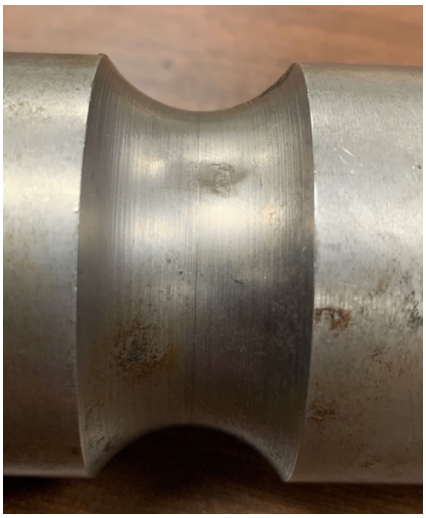

Figure 3.13: Unfractured loadcell Top Down View Showing Non-Central loading

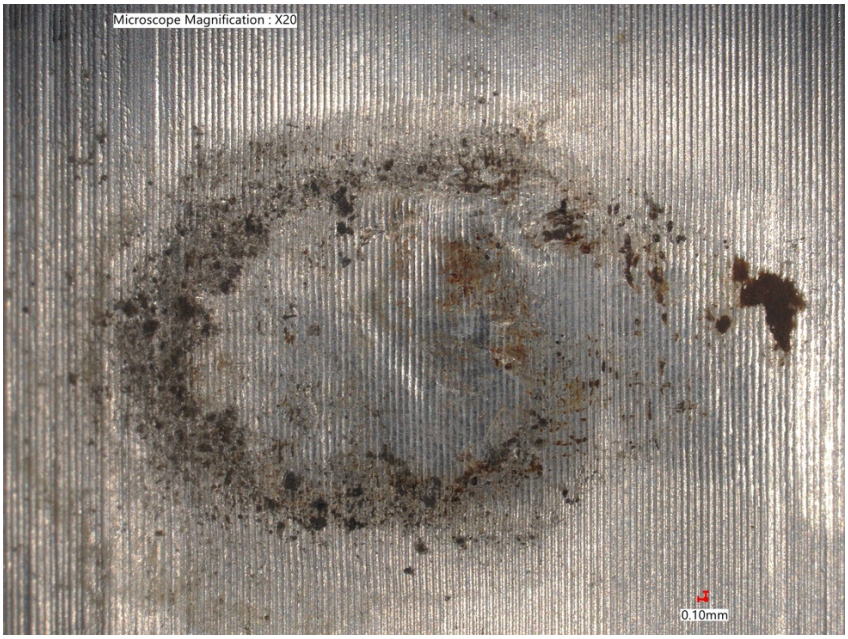

Figure 3.14: Fractured Loadcell Contact Region Top-Down View, VHX-7000 20X Magnification

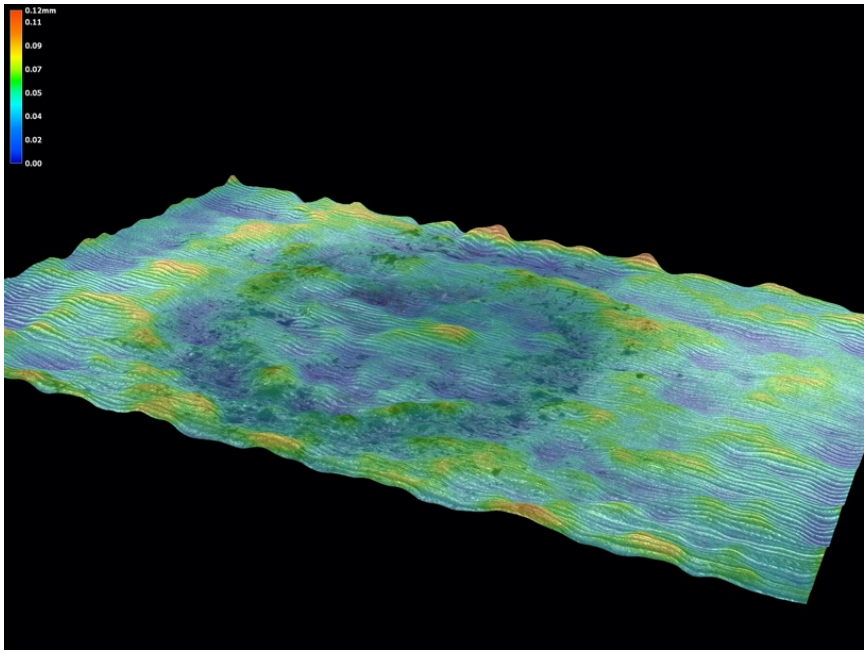

Figure 3.15: Color Depth Profile for Fractured Loadcell Contact Region, VHX-7000 20X Magnification

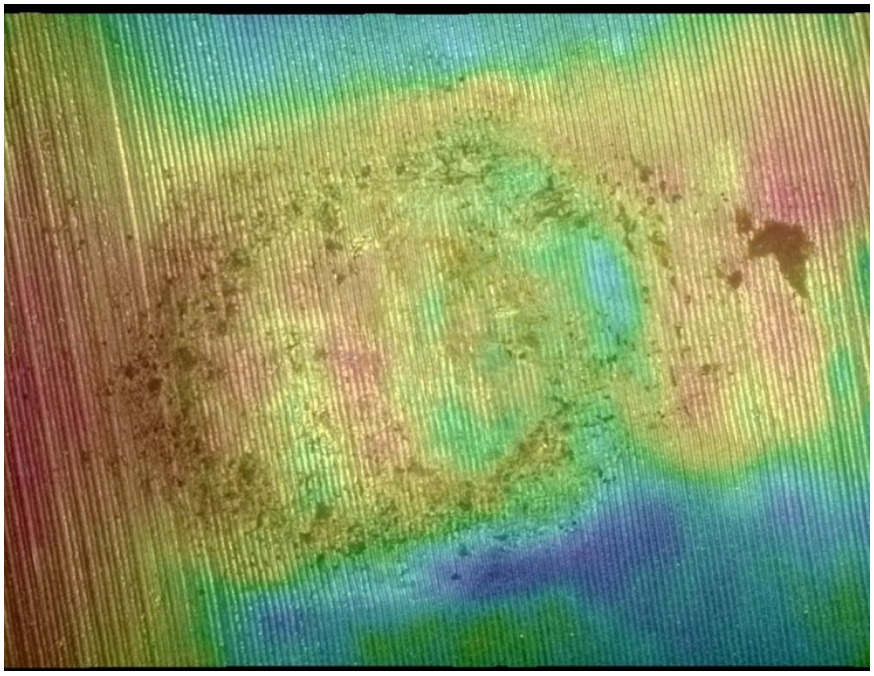

Figure 3.16: Fractured Loadcell Contact Region with Depth Color Plot, VHX-1000 30X Magnification

Upon analysis of the fractured loadcell color depth scans, it can be viewed that the contact surface is uneven. The red zones in figures 3.15, 3.16, and 3.19 are high zones and the blue zones are low zones relative to the rest of the depth. This unevenness in depth supports the idea that the force is applied through many low magnitude impacts between the bracket and the loadcell surface. An investigation of the unfractured loadcell should now be performed to fully compare the differences.

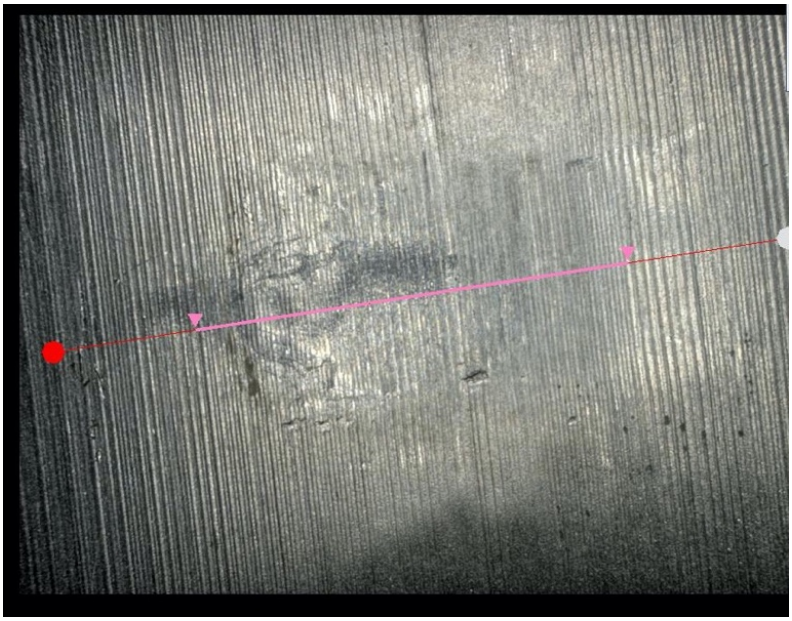

Figure 3.17: Unfractured Loadcell Contact Region, VHX-1000 30X Magnification

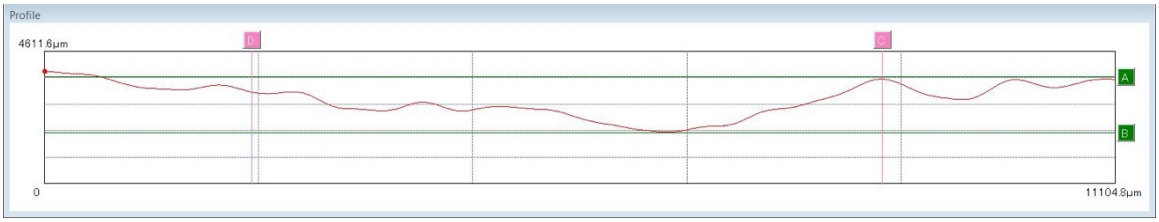

Figure 3.18: Profile for Unfractured Loadcell Contact Region, VHX-1000 30X Magnification

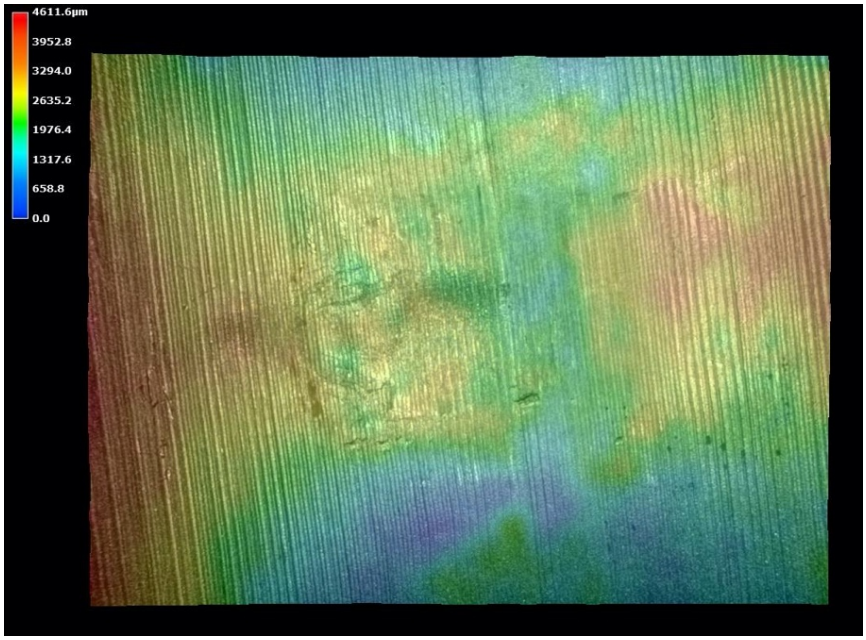

Figure 3.19: Unfractured Loadcell Color Depth Profile, VHX-1000 30X Magnification

An analysis of the unfractured loadcell contact region supports the theory that the surface fractures were caused by many small impacts as well. The profile of the region shown in figures 3.17 and 3.18 shows that the contact region is non-uniformly beaten in by these fractures. If it was a rubbing force, the profile would look more parabolic rather than spiked. Also, further investigation of the scans for all contact regions show that there are many different areas of non-uniform height within the contact region, indicating that the loadcell bracket made contact with the loadcell many times in slightly different locations rather than weathering it down at the same spot. This is indicative of impacts rather than rubbing.

4. CONCLUSION

4.1 WIND EXPERIMENTATION

The purpose of the wind experimentation was to prove that a wind loading will indeed cause an imbalance of weight within the supporting loadcells if its magnitude and direction attains critical values. By performing a dimensional analysis and scaling down the actual pressure vessels into models that can adequately represent them while also fitting within the 24 inch by 24 inch cross sectional opening of the wind tunnel and calculating scaled wind speeds that will correlate to wind speeds during dynamic wind loading conditions in real world operation. The test that was designed works by providing this proportional wind loading to the worst-case scenario of the pressure vessel models and testing it until there is a wind speed that induces instability in the pressure vessel in the form of excessive vibrations or toppling. To obtain a good range of results, the empty condition was tested with just the geometry and a mock catalyst was found through a mass equivalency to test the catalyst filled condition.

After performing the tests, the experimental toppling wind speeds were found and compared to the theoretical values. For the empty condition, the 50 Cuft, 200 Cuft, and 1100 Cuft pressure vessels started experiencing instability at 6.8 mph, 7.85 mph, and 9.06 mph respectively. The theoretical values for instability for such vessels are 6.6 mph, 6.8 mph, and 7.4 mph. This provides percent differences between the empty condition experimental and theoretical values 3.03%, 15.44%, and 22.43%. The catalyst-filled experimentation is similar. Here, the 50 Cuft, 200 Cuft, and 1100 Cuft pressure vessels started experiencing instability at 9.22 mph, 11.05 mph, and 11.83 mph respectively. The theoretical values for instability in the catalyst-filled condition for these vessels

respectively are 8.6 mph, 10.4 mph, and 12.4 mph. This provides percent differences between the empty condition experimental and theoretical values 7.21%, 6.25%, and 4.6%. As these experimental values are close to the theoretical values, this experiment confirms the theoretical values calculated for the life-sized pressure vessels are accurate for when the pressure vessel will experience instability and begin to impact the loadcells. As calculated, the pressure vessels will experience instability at 71.6 mph, 83.3 mph, and 88.0 mph for the empty condition and 89.7 mph, 126.6 mph, and 146.7 mph for the catalyst filled condition in the 50 Cuft, 200 Cuft, and 1100 Cuft respectively.

4.2 SURFACE IMAGING

The purpose of the surface imaging tests was to evaluate the fracture surfaces and points of interest within pressure vessel loadcells that had previously failed. There were multiple points of interest that were tested: the fracture surface, the surface cracks, and the contact regions between the loadcell brackets and the loadcells themselves. From looking at the loadcell face, the fracture can be determined as ductile due to the curvature and the roughness of the fractured faces. This means that the fracture occurred due to fatigue. Ductile breaks are rougher than brittle breaks as they are carried out over time and rather than in an instant. The fracture faces also revealed a discoloration in the face. This means the fracture happened in multiple stages, the first of which took a long time, allowing the weather as allowed to infiltrate the loadcell geometry, and the second of which was quicker than the first, probably taking a lesser amount of time as the majority of the cross section had already deteriorated. It also means that moisture and humidity were exposed to the internals of the loadcell geometry and time allowed them to leave a lasting imprint on the surface. The surface cracks on the non-fractured loadcell provided

more information on the beginning of the fracture. They show that surface cracking starts at the bottom and on the side of the loadcell and gradually spreads and widens across the bottom of the loadcell before moving towards the center. As these cracks widen, the moisture can infiltrate the internals of the cross section. Finally, the contact regions between the loadcell bracket and the loadcell itself show that the forces are applied via many low magnitude impacts caused by wind lifting the pressure vessel up and dropping it onto the load cell. This is the root cause of the fatigue failures seen in the fractured loadcell. All of these analysis support that the loadcell was a fatigue failure because the fracture was ductile, the contact region between the bracket and the loadcell is clearly indented due to many impacts, and the fractured face clearly progresses through all stages of a fatigue life failure: initialization, crack propagation, and catastrophic failure.

There are many opportunities for continued research in this field. Firstly, a drop test can be designed to confirm the depths of the surface cracks and develop a non-destructive test to determine the state of loadcells in the field without requiring a full dismantling of the pressure vessel. Also, a chemical analysis could be performed to date the oxidation on the lower surface of the fracture face. This can provide an accurate timeline for when the cracks start versus when the full fracture occurs.

WORKS CITED

[1] Clark, Christopher, “Measuring the Vortex-Shedding Frequency Behind Staggered Cylinders in Cross-Flow”(2018). *Santa Clara University*, 2018, pp. 1-2.

[2] Wolfendale, Peter C. F. 1986. Load Cells. United States of America.

[3] *“*Wind Forces.” 2015. VPG Transducers.

[4] Prapti Mahandari, Cokorda, and Aji Abdillah Kharismab. "Wind and earthquake loads on the analysis of a vertical pressure vessel for oil separator." (2015).

[5] Pressure Vessel Weighing Systems. Accessed November 20, 2019. https://www.ricelake.com/en-us/.

[6] Barenblatt, Grigory Isaakovich. 1996. “Scaling, self-similarity, and intermediate asymptotics.” Cambridge: Cambridge University Press.

[7] "Science Buddies: How to Build And Use A Subsonic Wind Tunnel". 2020. *Science Buddies*. https://www.sciencebuddies.org/science-fair-projects/references/how-to-build-a-wind-tunnel.

[8] “Keyence Digital Microscopes - VHX-1000 Series.” 2010. Keyence Corporation. Itasca, IL. Retrieved from https://www.keyence.com/products/microscope/digital-microscope/vhx-1000/downloads/.

[9] “Keyence Digital Microscopes - VHX-7000 Series.” 2010. Keyence Corporation. Itasca, IL.

[10] “How To Get The Most From A Digital Microscope.” 2019. Keyence Corporation. Itasca, IL.

[11] “Tips for Maximizing Microscope Usage.” 2019. Keyence Corporation. Itasca, IL.

[12] “AK Steel 17-4 PH® Precipitation Hardening Stainless Steel, Condition A.” MATWEB Material Property Data. Accessed October 28, 2020. http://www.matweb.com/search/datasheet.aspx?matguid=20362bbf0a7f45b8ae59b19a9425239e.

[13] Rack, H. J. “Physical and mechanical properties of cast 17-4 PH stainless steel.” No. SAND-80-2302; TTC-0161. Sandia National Labs., Albuquerque, NM (USA), 1981.

[14] Askeland, Donald R., Wendelin J. Wright, D. K. Bhattacharya, and R. P. Chhabra. “The Science and Engineering of Materials.” Boston, MA: Cengage Learning, 2016.

[15] Anderson, Ted L. “Fracture mechanics: fundamentals and applications.” CRC press, 2017.

[16] “ASM Handbook: Fractography.” Vol. 12. Materials Park, OH: ASM International, 1987.

[17] “The Potential Drop Technique & Its Use In Fatigue Testing.” 2020. Matelect LTD London, UK.

[18] Corcoran, Joseph, Catrin M Davies, Peter Cawley, and Peter B Nagy. “A Quasi-DC Potential Drop Measurement System for Material Testing.” *IEEE Transactions on Instrumentation and Measurement* 69 (May 14, 2020): 1313–26.

[19] Corcoran, Joseph, Peter B Nagy, and Peter Cawley. “Monitoring Creep Damage at a Weld Using a Potential Drop Technique.” *International Journal of Pressure Vessels and Piping* 153 (2017): 15–25.

[20] *Data of miscellaneous substances measured in density as per kg/m3, the substances include soils, metals, woods and liquids.* 2020. http://www.dust-monitoring-equipment.com/data.htm.

5. APPENDICES

APPENDIX A: DERIVATION OF DIMENSIONAL ANALYSIS VALUES FOR WIND SPEED

The first step in performing this dimensional analysis is to find the wind speeds that would be required to topple the full-sized vessels. In order to do this, the wind velocities increasing from 10 mph to 180 mph were converted to ft/s and were used to find the dynamic pressures, P, caused by each wind speed. 180 mph is roughly the top speed of a hurricane. This is shown by the below equation:

$$P = \frac{\rho v^2}{2} \quad [4]$$

Here, the Greek letter **ρ** represents the density of air and v represents the velocity of the air. After calculating dynamic pressures, the force, F, applied by this dynamic pressure was found. By finding the cross-sectional area at the widest point of the vessel and multiplying by the pressure, this force was found:

$$F = P * A \quad [5]$$

After finding the force that is applied by this dynamic pressure, it can be used to calculate a torque, T, that is being enacted at the base of each leg. This torque is found by multiplying the force calculated in the previous step by the total height minus ½ the diameter of the pressure vessel:

$$T = F * (L - 0.5D) \quad [6]$$

After finding the torque applied to each leg by the wind loading, the weight, W, that this dynamic loading applies to the loadcells can be calculated using the distance between the legs, Y, and the torque created by this dynamic loading, T:

$$W = T * Y \quad [7]$$

The following table was created to show the effects of different wind speeds on the full-sized pressure vessels.

Table 5.1: Weights Applied by Differing Wind Speeds on Full-Sized Pressure Vessels

	Wind Velocity (mph)	50 Cuft (lbs)	200 Cuft (lbs)	1100 Cuft (lbs)
1	10.0	28.6	44.9	133.1
2	20.0	114.2	179.7	532.2
3	30.0	257.0	404.4	1197.5
4	40.0	456.8	718.9	2129.0
5	50.0	713.8	1123.4	3326.5
6	60.0	1027.9	1617.6	4790.2
7	70.0	1399.0	2201.8	6520.0
8	80.0	1827.3	2875.8	8515.9
9	90.0	2312.7	3639.7	10777.9
10	100.0	2855.2	4493.4	13306.1
11	110.0	3454.8	5437.0	16100.4
12	120.0	4111.5	6470.5	19160.8
13	130.0	4825.3	7593.9	22487.3

Table 5.1: Weights Applied By Differing Wind Speeds on Full-Sized Pressure Vessels				
	Wind Velocity (mph)	50 Cuft (lbs)	200 Cuft (lbs)	1100 Cuft (lbs)
14	140.0	5596.2	8807.1	26079.9
15	150.0	6424.2	10110.2	29938.7
16	160.0	7309.3	11503.1	34063.6
17	170.0	8251.5	12985.9	38454.6
18	180.0	9250.8	14558.6	43111.7

In order to determine wind speed values that can be used, the same process was used using a span of wind speeds that the wind tunnel at Georgia Southern University is capable of producing; the wind speeds vary from 2 mph to 30 mph. Additionally, 18-inch test models were created with the size of the wind flow in mind. An 18-inch tall model allows for the center of gravity of the empty vessel to be directly in the center of the air flow as well as allowing the entire vessel body to be affected by the air. Using these updated dimensions and wind speeds, the following table was used to find equivalent force values that the wind will apply to each loadcell.

Table 5.2: Weights Applied by Differing Wind Speeds on 18-Inch Pressure Vessels				
	Wind Velocity (mph)	50 Cuft (lbs)	200 Cuft (lbs)	1100 Cuft (lbs)
1	2.0	0.0	0.0	0.0
2	4.0	0.0	0.0	0.0
3	6.0	0.1	0.1	0.1

Table 5.2: Weights Applied by Differing Wind Speeds on 18-Inch Pressure Vessels				
	Wind Velocity (mph)	50 Cuft (lbs)	200 Cuft (lbs)	1100 Cuft (lbs)
4	6.2	0.1	0.1	0.1
5	6.4	0.1	0.1	0.1
6	6.6	0.1	0.1	0.1
7	6.8	0.1	0.1	0.1
8	7.0	0.1	0.1	0.2
9	7.2	0.1	0.1	0.2
10	7.4	0.2	0.2	0.2
11	7.6	0.2	0.2	0.2
12	7.8	0.2	0.2	0.2
13	8.0	0.2	0.2	0.2
14	8.2	0.2	0.2	0.2
15	8.4	0.2	0.2	0.2
16	8.6	0.2	0.2	0.2
17	8.8	0.2	0.2	0.2
18	9.0	0.2	0.2	0.3
19	9.2	0.2	0.2	0.3
20	9.4	0.2	0.2	0.3
21	9.6	0.3	0.3	0.3
22	9.8	0.3	0.3	0.3

Table 5.2: Weights Applied by Differing Wind Speeds on 18-Inch Pressure Vessels				
	Wind Velocity (mph)	50 Cuft (lbs)	200 Cuft (lbs)	1100 Cuft (lbs)
23	10.0	0.3	0.3	0.3
24	10.2	0.3	0.3	0.3
25	10.4	0.3	0.3	0.3
26	10.6	0.3	0.3	0.3
27	10.8	0.3	0.3	0.4
28	11.0	0.3	0.3	0.4
29	11.2	0.4	0.3	0.4
30	11.4	0.4	0.4	0.4
31	11.6	0.4	0.4	0.4
32	11.8	0.4	0.4	0.4
33	12.0	0.4	0.4	0.4
34	12.2	0.4	0.4	0.5
35	12.4	0.4	0.4	0.5
36	12.6	0.4	0.4	0.5
37	12.8	0.5	0.5	0.5
38	13.0	0.5	0.5	0.5
39	13.2	0.5	0.5	0.5
40	13.4	0.5	0.5	0.6
41	13.6	0.5	0.5	0.6

Table 5.2: Weights Applied By Differing Wind Speeds on 18-Inch Pressure Vessels				
	Wind Velocity (mph)	50 Cuft (lbs)	200 Cuft (lbs)	1100 Cuft (lbs)
42	13.8	0.5	0.5	0.6
43	14.0	0.6	0.5	0.6
44	14.2	0.6	0.6	0.6
45	14.4	0.6	0.6	0.6
46	14.6	0.6	0.6	0.7
47	14.8	0.6	0.6	0.7
48	15.0	0.6	0.6	0.7
49	15.2	0.7	0.6	0.7
50	15.4	0.7	0.7	0.7
51	15.6	0.7	0.7	0.8
52	15.8	0.7	0.7	0.8
53	16.0	0.7	0.7	0.8
54	18.0	0.9	0.9	1.0
55	20.0	1.1	1.1	1.2
56	22.0	1.4	1.3	1.5
57	24.0	1.6	1.6	1.8
58	26.0	1.9	1.9	2.1
59	28.0	2.2	2.2	2.4
60	30.0	2.5	2.5	2.8

After these wind velocities have been found, the theoretical wind speed in which the pressure vessel model should experience toppling should be found. As there are pressure vessel legs each with a loadcell and they are all equidistant from each other, statically they hold the same amount of weight per loadcell. Therefore, the mass of the 18-inch model being tested is divided by 3 to figure out the weight. The point at which the pressure vessel will experience toppling is going to be when the force applied by the wind equals the amount of mass on each load cell**.** Through this theory, the heavier the pressure vessel is, the more wind loading that must be applied in order to visualize toppling. After looking at table 3.8 comparing the values of the weight of the vessel divided by 3 to the weight values here corresponding to the right vessel size, table 3.12 shows the wind speeds that the 18-inch should theoretically experience instability.

APPENDIX B: DERIVATION OF DENSITY REPLACEMENT EQUATION

In order to derive the required density for the 18-inch model, the requirements must be understood as such: The industrial pressure vessels have a particular mass and volume when empty and filled with fluid, and that weight and volume must be proportional to the mass and volume of the 18-inch model when both full and empty. Additionally, the density of the catalyst is a known variable. All variables denoted with a '1' are for the full-sized industrial vessel and the variables denoted with a '2' are for the 18-inch model. The following equations set up a mass ratio for the two situations. The empty weight of the vessel is required to be added because the mass that is available for calculation is the full weight of the vessel with fluid and shell.

$$m = \rho V \quad [8]$$

$$\frac{m_{full,2}}{m_{full,1}} = \frac{\rho_2 V_2 + m_{empty,2}}{\rho_1 V_1 + m_{empty,1}} \quad [9]$$

This leaves 2 unknown variables: the density of the fluid for the 18-inch model and the mass with fluid of the 18-inch model. Another mass relation is stated that the mass of the full vessel divided by the mass of the empty vessel must be proportional in both situations. This is then converted to solve for the full volume of the 18-inch model:

$$\frac{m_{full,1}}{m_{empty,1}} = \frac{m_{full,2}}{m_{empty,2}} \quad [10]$$

$$m_{full,2} = \frac{m_{full,1}}{m_{empty,1}} * m_{empty,2} \quad [11]$$

Combining these equations and solving for the required density provides the final equation below:

$$\rho_2 = \frac{\left(\frac{m_{empty,2}}{m_{empty,1}}\right) * \left(\rho_1 * V_{full,1} + m_{empty,1}\right) - m_{empty,2}}{V_{full,2}} \quad [3]$$

APPENDIX C: CONCAVE AND CONVEX PROFILES OF THE FRACTURED FACES (LANDSCAPE)